3-14-2006

Development of a Three-Dimensional Air Blast Propagation Model Based Upon the Weighted Average Flux Method

Stephen R. McHale

Recommended Citation

McHale, Stephen R., "Development of a Three-Dimensional Air Blast Propagation Model Based Upon the Weighted Average Flux Method" (2006). *Theses and Dissertations*. 3370.
https://scholar.afit.edu/etd/3370

DEVELOPMENT OF A THREE-DIMENSIONAL AIR BLAST PROPAGATION MODEL BASED UPON THE WEIGHTED AVERAGE FLUX METHOD

THESIS

Stephen R. McHale, Major, USA
AFIT/GNE/ENP/06-04

DEPARTMENT OF THE AIR FORCE
AIR UNIVERSITY

AIR FORCE INSTITUTE OF TECHNOLOGY

Wright-Patterson Air Force Base, Ohio

APPROVED FOR PUBLIC RELEASE; DISTRIBUTION UNLIMITED

AFIT/GNE/ENP/06-04

DEVELOPMENT OF A THREE-DIMENSIONAL AIR BLAST PROPAGATION MODEL BASED UPON THE WEIGHTED AVERAGE FLUX METHOD

THESIS

Presented to the Faculty

Department of Engineering Physics

Graduate School of Engineering and Management

Air Force Institute of Technology

Air University

Air Education and Training Command

in Partial Fulfillment of the Requirements for the

Degree of Master of Science (Nuclear Science)

Stephen R. McHale, BS

Major, USA

March 2006

AFIT/GNE/ENP/06-04

DEVELOPMENT OF A THREE-DIMENSIONAL AIR BLAST PROPAGATION MODEL BASED UPON THE WEIGHTED AVERAGE FLUX METHOD

Stephen R. McHale, BS
Major, USA

Approved:

Kirk A Mathews 14 Mar 06
Kirk A. Mathews Date

Raymond C. Maple 10 Mar 06
Raymond C. Maple Date

David W. Gerts 9 Mar 06
David W. Gerts Date

AFIT/GNE/ENP/06-04

Abstract

Accurate numerical modeling of complex, multi-dimensional shock propagation is needed for many Department of Defense applications. A three-dimensional code, based upon E.F. Toro's weighted average flux (WAF) method has been developed, tested, and validated. Code development begins with the introduction and application of all techniques in a single dimension. First-order accuracy is achieved via Godunov's scheme using an exact Riemann solver. Adaptive techniques, which employ approximate solutions, are implemented to improve computational efficiency. The WAF method produces second-order accurate solutions, but introduces spurious oscillations near shocks and contact discontinuities. Total variation diminishing (TVD) flux and weight limiting schemes are added to reduce fluctuation severity. Finally, the fully developed one-dimensional code is validated against experimental data, and extended into two and three dimensions via dimension-splitting techniques.

Acknowledgements

I would like to express sincere appreciation to my faculty advisor, Dr. Kirk Mathews, for his guidance, insight, and support throughout the course of this research effort. Furthermore, I thank my committee, Lt Col Raymond Maple and Maj David Gerts, for their time and support. I thank the members of the class of GNE 06-M who listened intently and provided constructive feedback during times of exaltation and lamentation alike. Finally, I thank my wife and family for keeping me encouraged, motivated, and, most importantly, well-loved.

Stephen R. McHale

Table of Contents

Page

List of Figures

Figure Page

List of Tables

Table Page

DEVELOPMENT OF A THREE-DIMENSIONAL AIR BLAST PROPAGATION MODEL BASED UPON THE WEIGHTED AVERAGE FLUX METHOD

1. Introduction

1.1. Motivation

The shock wave is an important natural phenomenon which commands attention. Accordingly, accurate and efficient numerical modeling of compressible, inviscid, time-dependent flow is a major branch of computational fluid dynamics. Analysis of complex, multi-dimensional shock propagation is an application of this numerical modeling and is needed for many Department of Defense (DoD) applications.

1.2. Background

Fluid dynamics is governed by a system of non-linear, hyperbolic partial differential equations which dictate conservation laws of mass, momentum, and energy. In 1952, Courant, Isaacson, and Rees introduced a first-order accurate scheme to solve these equations by finite differences. In 1959, Sergei K. Godunov presented an extension to this scheme which resolved a computational domain as a piecewise constant distribution of the conserved variables in a series of boundary value problems (Godunov, 1959:1187). These boundary value problems, known as Riemann problems, are solved exactly to satisfy the governing conservation laws and determine numerical fluxes of mass, momentum, and energy at each boundary. Godunov's method then applies these boundary fluxes to calculate the conserved variable values at either side of the boundary, which serve as conditions to solve Riemann problems, forward in time, as required.

Due to the non-linearity of the conservation laws, numerical iteration is required to obtain exact solutions to the Riemann problems. Since the introduction of Godunov's method, several approximate Riemann solvers have been developed that predict solutions without requiring computationally costly iteration. Unfortunately, Godunov's method, implemented with exact or approximate Riemann solvers, provides only first-order accuracy, making it unsuitable for application to practical problems where well-resolved solutions require fine meshes. Specifically, first-order schemes often result in smeared solutions at discontinuities, such as shock fronts, and predict slow convergence to these solutions (Toro, 1999:213).

In his text, *Riemann Solvers and Numerical Methods for Fluid Dynamics, 2d Edition*, E.F. Toro presents high-resolution, second-order techniques to remedy the shortcomings associated with first-order methods. Specifically, Toro's techniques permit determination of more accurate numerical fluxes at each boundary than Godunov's method allows. These fluxes are calculated by analyzing the wave structure of the Riemann problem to determine a weighted average of the flux vectors at the boundary. While Toro's weighted average flux (WAF) method improves accuracy, it also introduces false fluctuations at discontinuities, such as shock fronts. Toro ultimately applies total variation diminishing (TVD) techniques to limit the flux weights and resolve these discontinuities in the regions of interest. Finally, Toro's methods may be applied to solve single or multi-dimensional problems (Toro, 1999:490).

1.3. Problem

The principal endeavor of this research is the development of a three-dimensional hydrodynamic shock code to solve the Euler conservation equations based upon the weighted average flux method (Toro, 1999:492). The secondary objective applies the developed code to model air blast propagation in one, two, and three dimensions.

1.4. Scope

The developed computational model is limited to modeling air blast under ideal conditions.

1.5. Assumptions and Limitations

The numerical hydrodynamics code assumes air behaves as an ideal gas with a constant ratio of specific heats ($\gamma = 1.4$). This assumption limits application of the code to low and intermediate pressure regions where peak pressures remain below 100 psi (690 kPa). Modeling of air blast propagation assumes that the atmosphere is homogeneous, with sea level properties, up to 5000 feet (Glasstone and Dolan: 103). The model also assumes the earth behaves as an ideal surface which is flat and reflects all incident energy.

1.6. Approach

Accurate and efficient one-dimensional numerical hydrodynamics modeling serves as the basis for code development in two and three dimensions. An algorithm to solve a single Riemann problem for the Euler conservation equations, exactly, was developed first. Next, a Godunov's method algorithm applied the exact Riemann solver to an entire computational domain, providing first-order accuracy. Godunov's algorithm then incorporated three approximate Riemann solvers, in order to maximize computational efficiency. Application of Toro's WAF method followed and provided second-order accurate solutions, while four TVD weight limiters were incorporated to reduce false fluctuations at discontinuities. During each step of code development, numerical values of the physical variables of density, material speed, and pressure, as well as internal energy, were verified against five documented shock tube tests using a fine mesh of 10001 points over a domain length of one meter for the exact Riemann solver, and a coarse mesh of 200 points for each of the Godunov method algorithms. Finally, the second-order accurate Godunov WAF TVD model was validated against the Army Research Laboratory (ARL) 57cm shock tube test using a mesh of 5000 points over 50 meters.

Following validation of the one-dimensional model, the code was extended into two and three dimensions by dimension splitting techniques. The two and three-dimensional codes were verified against mild cylindrical and spherical shock tests presented by Toro.

2. Fluid Dynamics Theory

2.1. Governing Equations

The laws of conservation of mass, momentum, and energy as applied to fluid motion are summarized, comprehensively, by a set of non-linear partial differential equations known as the Navier-Stokes equations. For mathematical and experimental reasons, the boundary conditions which accompany these computationally precise equations dictate solution procedures which are often inefficient and impractical. However, application of some simplifying assumptions reduces these complex equations to a simpler set of partial differential equations, commonly referred to as the Euler equations (Chorin and Marsden, 1990:34).

2.2. Simplifying Assumptions

The Euler equations result from the assumptions that viscosity, heat conduction, and body forces are negligible for a compressible medium. If these assumptions are maintained by the computational model that simulates shock propagation through air and shock reflection at a surface, then the Euler equations may be justifiably applied to this model. Therefore, an analysis of viscosity, heat conduction, and body forces within the air, at the boundary between the air and surface, and at the surface where shock interaction occurs is necessary.

The computational model assumes a homogeneous atmosphere with sea-level properties. Regarding air located far from a boundary, this assumption implies negligible density, velocity, and temperature gradients exist, and justifies ignoring body forces, viscosity, and heat conduction, respectively.

The model also assumes that the earth behaves as an ideal surface that is flat and reflects all incident energy, which allows heat conduction between the air and the surface to be ignored. Furthermore, shocks propagating over this smooth, flat surface exert high pressures and inertias over a physical domain that is large in comparison to the thin surface boundary. Therefore, variations in pressure normal to the surface are negligible within the boundary layer, which indicates the pressure distribution at the surface results from the flow above the boundary. Hence, viscosity at the boundary between the air and surface can also be ignored. Finally, because viscosity and heat conduction may be ignored within air located far from a boundary, and at the boundary between the air and the ideal surface, the air at these locations is characterized as inviscid and adiabatic (Wittig, 1999:5).

Examination of air located at the shock front indicates this air is neither inviscid nor adiabatic. Physically, a shock front represents a thin region where the properties of density, pressure, and material velocity change rapidly. The temperature and velocity gradients incurred at the front imply viscosity, heat transfer, and entropy cannot be ignored, and the simplifying assumptions that allow reduction of the Navier-Stokes equations to the Euler equations are effectively threatened. However, if the physical shock front is represented, mathematically, as a discontinuity, and the width of this discontinuity is assumed to be small with respect to the domain represented by the computational model, and the second law of thermodynamics sufficiently recognizes the discontinuity and predicts physically correct behavior at the shock front, then viscosity and heat conduction may be neglected at the front, as an approximation. In fact, smooth solutions obtained from the Navier-Stokes equations compared to discontinuous solutions obtained by applying simplifying assumptions are nearly indistinguishable (LeVeque, 1992:9).

The assumptions that air viscosity, heat conduction, and body forces are negligible justify applying the Euler equations to the developed computational model.

2.3. The Euler Equations

The time-dependent Euler form of the conservation equations of mass, momentum, and energy may be written in compact vector notation as

$$\mathbf{U}_t + \mathbf{F}(\mathbf{U})_x + \mathbf{G}(\mathbf{U})_y + \mathbf{H}(\mathbf{U})_z = \mathbf{0} \tag{2.1}$$

where $\mathbf{U}$ is a column vector of conserved variable densities and $\mathbf{F}(\mathbf{U})$, $\mathbf{G}(\mathbf{U})$, and $\mathbf{H}(\mathbf{U})$ represent fluxes of conserved variables in the x, y, and z directions, respectively, as

$$\mathbf{U} = \begin{bmatrix} \rho \\ \rho u \\ \rho v \\ \rho w \\ E \end{bmatrix} \tag{2.2}$$

and

$$\mathbf{F} = \begin{bmatrix} \rho u \\ \rho u^2 + p \\ \rho uv \\ \rho uw \\ u(E+p) \end{bmatrix}, \qquad \mathbf{G} = \begin{bmatrix} \rho v \\ \rho vu \\ \rho v^2 + p \\ \rho vw \\ v(E+p) \end{bmatrix}, \qquad \mathbf{H} = \begin{bmatrix} \rho w \\ \rho wu \\ \rho wv \\ \rho w^2 + p \\ w(E+p) \end{bmatrix}. \tag{2.3}$$

Vectors are denoted by boldface letters. The subscript t in equation (2.1) represents a temporal partial derivative, while subscripts x, y, and z symbolize spatial partial derivatives (Toro, 1999:3).

Two sets of variables, conserved and primitive, are used in the conservation equations, and there exists some freedom when choosing variables to describe the flow under consideration. Conserved variables represent conserved quantities of mass, momentum, and energy, while the primitive variables of density, velocity, and pressure can be easily measured and are often imposed by the domain of the problem. Algebraic simplification and application of the ideal gas equation of state, discussed in Section 2.4, allows the primitive variables to be expressed in terms of the conserved variables, or vice versa, where

$$\mathbf{W} \equiv \begin{bmatrix} \rho \\ u \\ v \\ w \\ p \end{bmatrix} = \begin{bmatrix} \rho \\ \rho u / \rho \\ \rho v / \rho \\ \rho w / \rho \\ (\gamma - 1)(E - (\frac{\rho}{2}(u^2 + v^2 + w^2))) \end{bmatrix}. \tag{2.4}$$

In a single dimension, assuming uniform flows in the y and z directions, equation (2.1) may be written

$$\mathbf{U}_{\boldsymbol{t}} + \mathbf{F}(\boldsymbol{U})_x = \mathbf{0} \tag{2.5}$$

where

$$\mathbf{U} = \begin{bmatrix} \rho \\ \rho u \\ E \end{bmatrix}, \quad \mathbf{F} = \begin{bmatrix} \rho u \\ \rho u^2 + p \\ u(E + p) \end{bmatrix}. \tag{2.6}$$

Similarly, a two-dimensional analysis where uniform flow exists in the z-direction requires solving

$$\mathbf{U}_t + \mathbf{F}(\mathbf{U})_x + \mathbf{G}(\mathbf{U})_y = \mathbf{0} \tag{2.7}$$

where

$$\mathbf{U} = \begin{bmatrix} \rho \\ \rho u \\ \rho v \\ E \end{bmatrix}, \quad \mathbf{F} = \begin{bmatrix} \rho u \\ \rho u^2 + p \\ \rho uv \\ u(E + p) \end{bmatrix}, \quad \mathbf{G} = \begin{bmatrix} \rho v \\ \rho vu \\ \rho v^2 + p \\ v(E + p) \end{bmatrix}. \tag{2.8}$$

Examination of the single or multi-dimensional Euler equations reveals, in all cases, that the number of unknown variables exceeds the number of equations by one. Therefore, an appropriate thermodynamic equation of state relating two or more physical quantities within the medium is required to guarantee a solution for all unknown variables.

2.4. Thermodynamic Considerations

The energy density, E, included in equation (2.2) is expressed

$$E = \frac{1}{2}\rho(u^2 + v^2 + w^2) + \rho e \tag{2.9}$$

where e is specific internal energy. Assuming the medium within the computational model behaves as a calorically ideal gas, then the density and pressure within the medium are related by the ideal gas equation of state (EOS):

$$p = \rho R T \tag{2.10}$$

where R is the universal gas constant and T is the temperature. If the ideal gas EOS is assumed, then it follows that internal energy is a function of temperature alone, or

$$e = c_v T \tag{2.11}$$

where c_v ,the specific heat capacity at constant volume, is a constant. Furthermore,

$$c_p - c_v = R \tag{2.12}$$

where c_p ,the specific heat capacity at constant pressure, is also constant.

Defining the ratio of specific heats, γ , as

$$\gamma \equiv \frac{c_p}{c_v} \tag{2.13}$$

and substituting equations (2.11) and (2.12) into equation (2.10) yields the relationship

$$e = \frac{p}{\rho(\gamma - 1)}. \tag{2.14}$$

Substitution of (2.14) into (2.9) presents a relationship for E in terms of the primitive variables $\rho, u, v, w,$ and p and provides necessary closure to the system of Euler conservation equations (Toro, 1999:13).

3. Exact Riemann Solver Development

3.1. The Riemann Problem for the Euler Equations

The Riemann problem (RP) for the one-dimensional time-dependent Euler conservation equations is the initial value problem (IVP)

$$\left.\begin{array}{l} \mathbf{U}_t + \mathbf{F}(\mathbf{U})_x = \mathbf{0} \\ \mathbf{U} = \begin{bmatrix} \rho \\ \rho u \\ E \end{bmatrix}, \ \mathbf{F} = \begin{bmatrix} \rho u \\ \rho u^2 + p \\ u(E+p) \end{bmatrix}, \end{array}\right\} \tag{3.1}$$

with initial conditions

$$\boldsymbol{U}(x,0) = \boldsymbol{U}^{(0)}(x) = \begin{cases} \boldsymbol{U}_\mathrm{L} & x < 0 \\ \boldsymbol{U}_\mathrm{R} & x > 0 \end{cases}. \tag{3.2}$$

The domain of interest in the x-t plane is the set of points $(x,\ t)$ where $-\infty < x < \infty$ and $t > 0$. In practice, x varies in a finite interval $[x_L, x_R]$ around the point $x = 0$. Additionally, the vector of primitive variables at a specified time $\mathbf{W} = (\rho, u, p)^T$ is frequently used when solving the RP, as opposed to the vector $\mathbf{U}$ of conserved variables. Therefore, the RP is the IVP for (3.1) consisting of constant data states $\mathbf{W}_\mathrm{L}$ and $\mathbf{W}_\mathrm{R}$ left and right of a discontinuity located at $x = 0$.

Physically, as applied to the Euler equations, the RP represents a simplified shock tube problem. In this problem, two stationary gases are initially separated by a boundary. Removal of this boundary generates a nearly centered system of three waves that typically consists of a rarefaction wave, contact discontinuity, and a shock wave (Toro, 1999:117; Ben-Artzi, 2003:98).

3.2. The Riemann Problem Wave Structure

Figure 3.1 depicts one example of a Riemann problem wave structure. Solutions to the system of partial differential equations in the IVP (3.1) produce three wave families associated with the eigenvalues listed above each wave number in Figure 3.1. For each eigenvalue, u is the material velocity and a represents the local speed of sound.

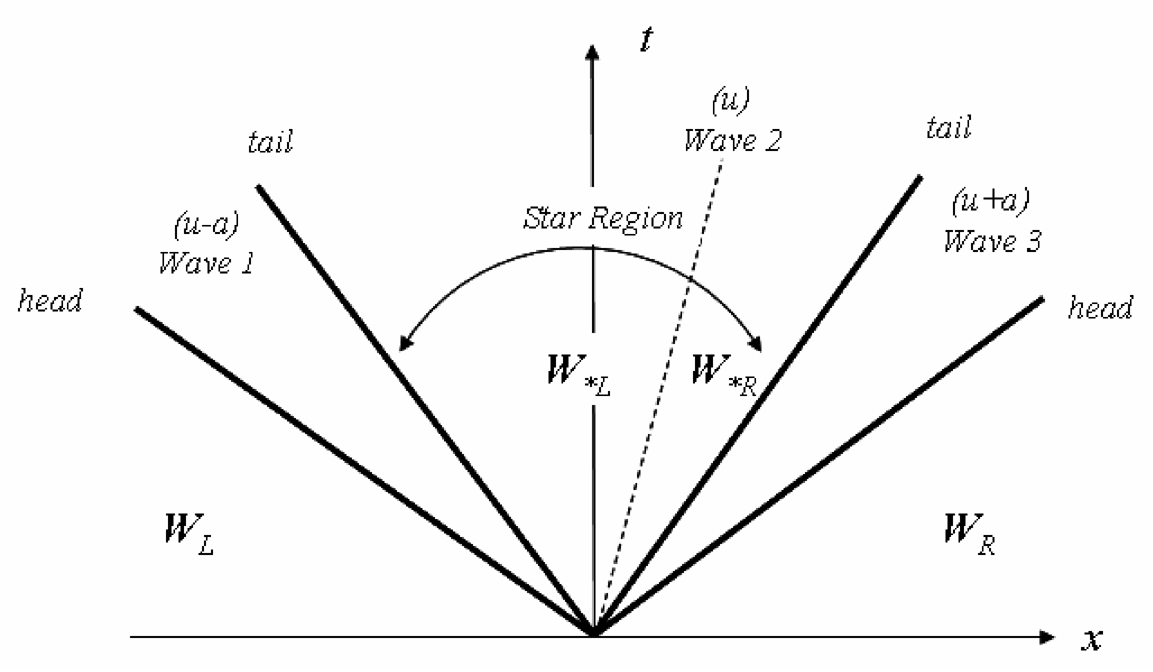

Figure 3.1. Riemann Problem Wave Structure

As indicated in the figure, the wave families effectively separate the RP, from left to right, into four regions $\mathbf{W}_{\mathrm{L}}, \mathbf{W}_{*\mathrm{L}}, \mathbf{W}_{*\mathrm{R}}$, and $\mathbf{W}_{\mathrm{R}}$. Although the left and right most states are known based on the initial conditions specified in the RP, information about the star region is necessary in order to fully define the RP. Solutions dictate waves one and three may be classified as shocks or rarefactions, while wave two is always a contact surface wave. Traditionally, a rarefaction is represented as a pair of rays, with a head and tail, while shocks are depicted by a single, solid line. Until the full classification of the outer waves as shocks or rarefactions occurs, both waves are portrayed as rarefactions. Consequently, accurate identification of waves one and three as shocks or rarefactions must occur before full definition of the RP, and the method of characteristics provides the ability to accomplish this identification.

3.3. The Method of Characteristics

Characteristic vectors, often called eigenvectors, provide straight-line solutions to a system of linear differential equations. Analysis of these vectors facilitates generation of characteristic fields, which provide qualitative information about the behavior of a system of equations (Blanchard, 2002:258). Unfortunately, the Euler equations are non-linear, resulting in discontinuities where characteristics cross (Wittig, 1999:14). Nevertheless, the method of characteristics generates useful qualitative information and accurately identifies RP waves as shocks, rarefactions, or contact surface waves. This classification, coupled with known information from the left and right states specified by the initial conditions facilitates solution for variables in the star region and, ultimately, completes solution for variables in all four RP regions.

Recall that properties of density, material velocity, and pressure are mathematically discontinuous for a shock wave. Conversely, a rarefaction wave is a smooth wave region where solutions for the same properties vary continuously between the head and tail. A characteristic vector field associated with a right moving rarefaction is depicted in Figure 3.2. The divergent characteristics within the fan and on either side of the wave indicate pressure and density decrease across the expansion fan from head to tail, while material velocity also decreases. A left moving rarefaction exhibits identical behavior, except for material velocity, which increases across the expansion fan from head to tail. In both cases, the speed of the head represents the speed of the rarefaction wave.

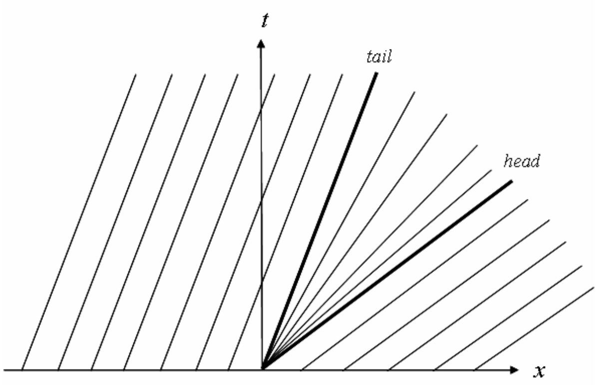

Figure 3.2. Characteristic Field of a Right Moving Rarefaction

Figure 3.3 depicts a characteristic vector field associated with a left moving shock. Along the line where characteristics cross, solutions are discontinuous. Accordingly, properties of density, material velocity, and pressure experience an instantaneous jump across the wave from head to tail.

Graphically, the head and tail are conventionally removed and the shock wave is represented by a bold, solid line. Finally, the speed of the head does not represent shock speed, as the shock wave cannot be classified characteristic. This shock speed will be analyzed later.

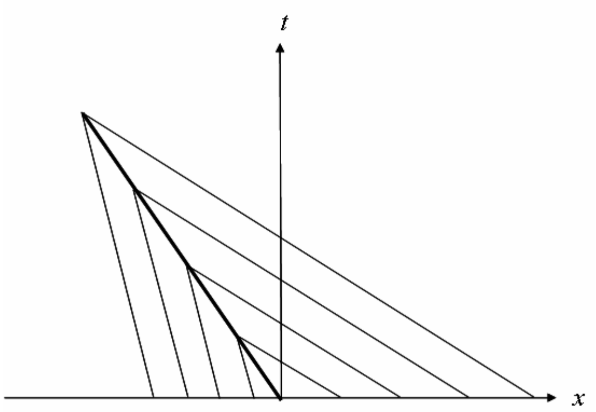

Figure 3.3. Characteristic Field of a Left Moving Shock

Recall the center wave in the RP structure is always a contact surface wave. Figure 3.4 shows the characteristic vector field is parallel to the contact surface.

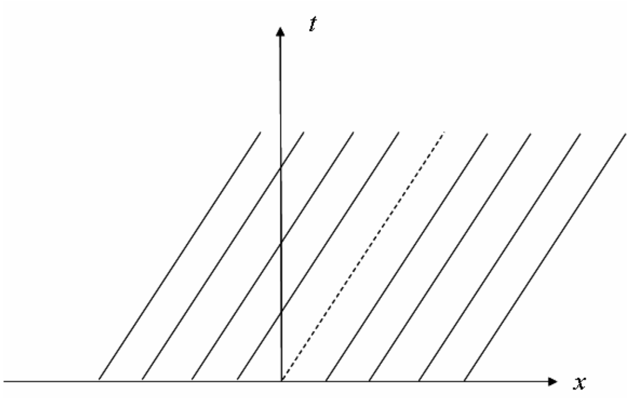

Figure 3.4. Characteristic Field of a Right Moving Contact Surface

In the context of the RP, both pressure and material velocity are constant across wave two as

$$p_{*\mathrm{L}} = p_{*\mathrm{R}} = p_{*}, \qquad (3.3)$$
$$u_{*\mathrm{L}} = u_{*\mathrm{R}} = u_{*},$$

while density experiences a jump across the contact surface and

$$\rho_{*\mathrm{L}} \neq \rho_{*\mathrm{R}} . \qquad (3.4)$$

Classification of waves one and three as shocks or rarefactions, together with primitive variable information from states $\mathbf{W}_{\mathrm{L}}$ and $\mathbf{W}_{\mathrm{R}}$ provides necessary information to solve for $\mathbf{W}_{*\mathrm{L}}$ and $\mathbf{W}_{*\mathrm{R}}$ and fully define the RP. The exact Riemann solver (ERS) provides the method to accomplish this task.

3.4. The Exact Riemann Solver (ERS)

3.4.1. Solution Strategy

As a pedagogical exercise, Toro applies the ERS to a simplified shock tube problem. Specifically, the shock tube is treated as a single RP, with a diaphragm separating constants states left and right of the boundary. Methods for determining the values of primitive variables in the star region are presented. Following solution for these variables in all four RP states, primitive variable values are calculated at a user specified number of points within the shock tube. Toro refers to this second step as sampling. While this method is a simplified approach to shock tube modeling, the solution of a single RP serves as the basis for subsequent methods which treat a computational domain as a series of local Riemann problems.

3.4.2. Calculation of Star Variables

Toro's process to connect known and unknown states is straight-forward. Material velocities in the left and right star states are determined using the equations

$$\begin{aligned} u_{*\mathrm{L}} &= u_{\mathrm{L}} - f_{\mathrm{L}}(p_*, \boldsymbol{W}_{\mathrm{L}}), \\ u_{*\mathrm{R}} &= u_{\mathrm{R}} + f_{\mathrm{R}}(p_*, \boldsymbol{W}_{\mathrm{L}}). \end{aligned} \tag{3.5}$$

The functions f_{L} and f_{R} are dependent on the classification of the left and right waves. If the outer wave is a shock, the Rankine-Hugoniot conditions are applied to determine the functions. On the other hand, if the outer wave is a rarefaction, isentropic relationships and the Generalized Riemann Invariants along the characteristics are used (Toro, 1999:120). A generalized pressure function, $f_\xi(p_*, \mathbf{W}_\xi)$, where ξ indicates the appropriate left or right state, results as

$$f_\xi(p_*, \mathbf{W}_\xi) = \begin{cases} (p_* - p_\xi)\left(\dfrac{2}{\rho_\xi(p_*(\gamma+1) + \rho_\xi(\gamma-1))}\right)^{\frac{1}{2}} & \textit{if} \quad p_* > p_\xi \ \textit{(shock)}, \\ \dfrac{2a_\xi}{\gamma-1}\left[\left(\dfrac{p_*}{p_\xi}\right)^{\frac{\gamma-1}{2\gamma}} - 1\right] & \textit{if} \quad p_* \le p_\xi \ \textit{(rarefaction)}. \end{cases} \tag{3.6}$$

It follows from (3.3) that within the star region $u_{*\mathrm{L}} - u_{*\mathrm{R}} = 0$. Applying this relationship to (3.5) yields the equation

$$f_L(p_*, \mathbf{W}_\mathrm{L}) + f_R(p_*, \mathbf{W}_\mathrm{R}) + u_\mathrm{R} - u_\mathrm{L} = 0 \tag{3.7}$$

whose root, p_*, must be found. The process for determining numerically p_* is, at this point, uncomplicated. First, an initial guess for p_* is generated. Next, the generated value is substituted into (3.6) in order to determine $f_\mathrm{L}(p_*, \mathbf{W}_\mathrm{L})$ and $f_\mathrm{R}(p_*, \mathbf{W}_R)$. Finally, the condition defined in (3.7) is verified against a specified tolerance. If the condition is satisfied the process is complete, but if the condition fails, the process is repeated.

Newton's method was chosen as the root finding algorithm due to its quadratic convergence to a solution and ease of implementation. Toro facilitates incorporating this algorithm by providing explicit derivatives for the pressure functions, which Newton's method requires, and by presenting techniques which generate initial guesses for p_*, based on known primitive variable information from the left and right states.

After determining pressure in the star region, the solution for u_* follows (Toro, 1999:119) as

$$u_* = \frac{1}{2}(u_\mathrm{L} + u_\mathrm{R}) + \frac{1}{2}\left[f_\mathrm{R}\left(p_*, \boldsymbol{W}_\mathrm{R}\right) + f_\mathrm{L}\left(p_*, \boldsymbol{W}_\mathrm{L}\right)\right] \tag{3.8}$$

Recall within the star region $\rho_{*\mathrm{L}} \neq \rho_{*\mathrm{R}}$. The values for density within this region depend on the classification of the wave and are determined via the generalized density function $\rho_{*\xi}(p_*, p_\xi, \rho_\xi)$, where ξ indicates the appropriate left or right state (Toro, 1999:133), as

$$\rho_{*\xi}(p_*, p_\xi, \rho_\xi) = \begin{cases} \rho_\xi \left(\dfrac{p_*(\gamma+1) + p_\xi(\gamma-1)}{p_*(\gamma-1) + p_\xi(\gamma+1))} \right) & \mathit{if} \;\; p_* > p_\xi \;\; \mathit{(shock)}, \\ \rho_\xi \left(\dfrac{p_*}{p_\xi} \right)^{\frac{1}{\gamma}} & \mathit{if} \;\; p_* \le p_\xi \;\; \mathit{(rarefaction)}. \end{cases} \tag{3.9}$$

Solution for primitive variables in the star region is complete, and the RP is fully defined.

3.4.3. Sampling

Sampling determines the exact solution to the RP at any point (*x, t*) in the domain of interest. The procedure makes use of an important mathematical property that states, along straight rays emanating from the origin ($x = 0$), solutions to the RP are self-similar (Ben-Artzi, 2003:99). Solutions at different time instants are obtained from one another by a similarity transformation, which is analogous to scaling. In short, the knowledge of the RP solution at an instant in time t_0 is sufficient to obtain a solution for all $t > 0$ (Polyanin, 2004:695).

The physical domain for the shock tube problem is [0, *L*] x [0, *T*] where *T* is the specified solution time. To guarantee self-similarity within the problem, the discontinuity, physically located at $x = L/2$ in the shock tube coordinate system, must be transformed to $x' = 0$, where x' represents the location in the

RP coordinate system. Figure 3.5 illustrates that the coordinate transformation occurs for all points x' as

$$x' = x - \frac{L}{2}\,. \tag{3.10}$$

It follows that the speed required to reach a point x' at time t in the RP coordinate system is

$$s' = \frac{x'}{t}. \tag{3.11}$$

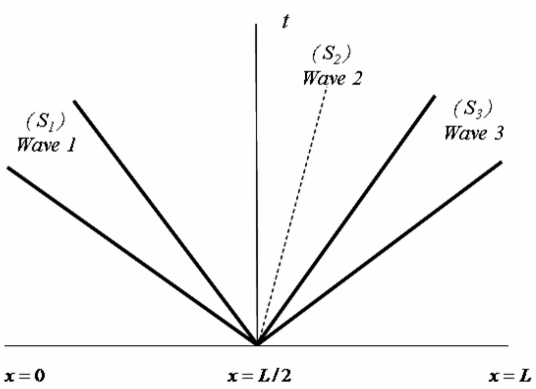

Figure 3.5a. Shock Tube Coordinates

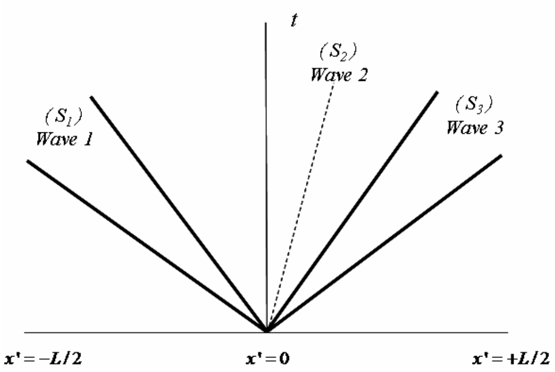

Figure 3.5b. RP Coordinates

A solution for the primitive variables at the point (x', t) is obtained by comparing s' to the three RP wave speeds. These wave speeds are determined by the set of equations

$$S_1 = \begin{cases} u_{\mathrm{L}} - a_{\mathrm{L}} \left[\dfrac{\gamma+1}{2\gamma} \left(\dfrac{p_*}{p_{\mathrm{L}}} \right) + \dfrac{\gamma-1}{2\gamma} \right]^{\frac{1}{2}} & \textit{if } p_* > p_L \textit{ (shock)}, \\ u_{\mathrm{L}} - a_{\mathrm{L}} & \textit{if } p_* \leq p_L \textit{ (rarefaction)}, \end{cases}$$

$$S_2 = u_*, \tag{3.12}$$

$$S_3 = \begin{cases} u_{\mathrm{R}} + a_{\mathrm{R}} \left[\dfrac{\gamma+1}{2\gamma} \left(\dfrac{p_*}{p_{\mathrm{R}}} \right) + \dfrac{\gamma-1}{2\gamma} \right]^{\frac{1}{2}} & \textit{if } p_* > p_R \textit{ (shock)}, \\ u_{\mathrm{R}} + a_{\mathrm{R}} & \textit{if } p_* \leq p_R \textit{ (rarefaction)}. \end{cases}$$

If a left rarefaction is present, then the speeds of the head and tail are calculated as

$$\begin{aligned} S_{\mathrm{HL}} &= u_{\mathrm{L}} - a_{\mathrm{L}}, \\ S_{\mathrm{TL}} &= u_{*\mathrm{L}} - a_{*\mathrm{L}}. \end{aligned} \tag{3.13}$$

For a right rarefaction, the head and tail move with speeds

$$\begin{aligned} S_{\mathrm{HR}} &= u_{\mathrm{R}} + a_{\mathrm{R}}, \\ S_{\mathrm{TR}} &= u_{*\mathrm{R}} + a_{*\mathrm{R}}, \end{aligned} \tag{3.14}$$

where

$$a_{*\xi} = a_\xi \left(\frac{p_*}{p_\xi} \right)^{\frac{\gamma-1}{2\gamma}}. \tag{3.15}$$

At this point, all necessary information to determine $\mathbf{W}(x', t)$ exists. Because u_* represents the contact surface wave speed, comparison of s' to u_* determines if the sample point is located left or right of the contact discontinuity.

Specifically, if $s' < u_*$ the sample point is located left of the contact.

Conversely, the point is right of the contact wave when $s' > u_*$.

Figure 3.6 shows when the sample point (x', t) lies left of a contact discontinuity, and in the presence of a shock, primitive variables are determined as

$$\mathbf{W}(x',t)=\begin{cases}\mathbf{W}_{\mathrm{L}} & \mathit{if}\ \dfrac{x'}{t}\le S_{\mathrm{L}},\\[2ex] \mathbf{W}_{*\mathrm{L}} & \mathit{if}\ S_{\mathrm{L}}\le \dfrac{x'}{t}\le u_* .\end{cases} \tag{3.16}$$

On the other hand, in the presence of a rarefaction, primitive variables are calculated as

$$\mathbf{W}(x',t)=\begin{cases}\mathbf{W}_{\mathrm{L}} & \mathit{if}\ \dfrac{x'}{t}\le S_{\mathrm{HL}},\\[2ex] \mathbf{W}_{\mathrm{L}\,\mathit{fan}} & \mathit{if}\ S_{\mathrm{HL}}\le \dfrac{x'}{t}\le S_{\mathrm{TL}},\\[2ex] \mathbf{W}_{*\mathrm{L}} & \mathit{if}\ S_{\mathrm{TL}}\le \dfrac{x'}{t}\le u_* .\end{cases} \tag{3.17}$$

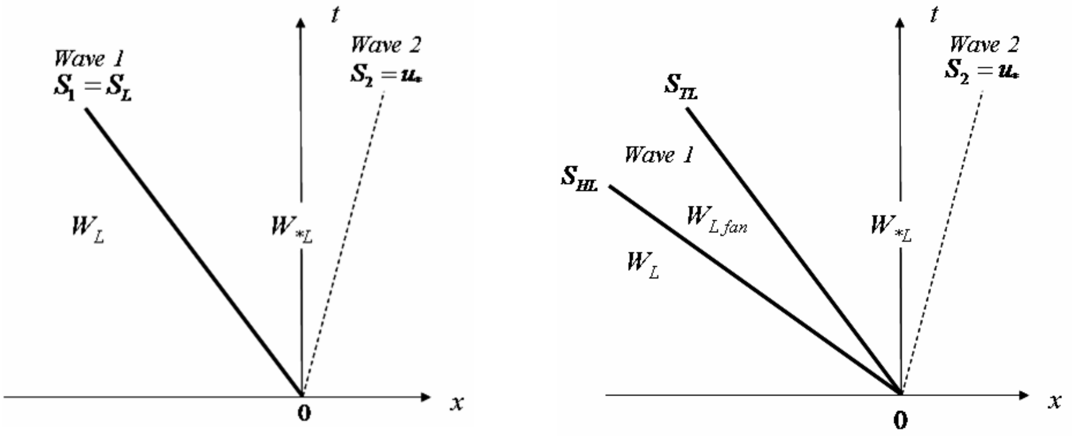

Figure 3.6. Sampling a Solution Point Left of the Contact

Because primitive variables vary continuously within the rarefaction expansion fan, calculation of these variables requires special consideration as (Toro, 1999:135)

$$\mathbf{W}_{\mathrm{L}\,fan}(\mathbf{W}_{\mathrm{L}},\, x',\, t) = \begin{cases} \rho = \rho_{\mathrm{L}}\left[\dfrac{2}{\gamma+1} + \dfrac{\gamma-1}{a_{\mathrm{L}}(\gamma+1)}(u_{\mathrm{L}} - \dfrac{x'}{t})\right]^{\frac{2}{\gamma-1}}, \\ u = \dfrac{2}{\gamma+1}\left[a_{\mathrm{L}} + \dfrac{(\gamma-1)}{2}u_{\mathrm{L}} + \dfrac{x'}{t}\right], \\ p = p_{\mathrm{L}}\left[\dfrac{2}{\gamma+1} + \dfrac{\gamma-1}{a_{\mathrm{L}}(\gamma+1)}(u_{\mathrm{L}} - \dfrac{x'}{t})\right]^{\frac{2\gamma}{\gamma-1}}. \end{cases} \tag{3.18}$$

The same analysis occurs when determining primitive variable values for a point (x', t) right of a contact surface discontinuity. Figure 3.7 shows, in the presence of a shock, primitive variables are calculated by

$$\mathbf{W}(x', t) = \begin{cases} \mathbf{W}_{*\mathrm{R}} & \text{if } u_* \leq \dfrac{x'}{t} \leq S_{\mathrm{R}}, \\ \mathbf{W}_{\mathrm{R}} & \text{if } \dfrac{x'}{t} \geq S_{\mathrm{R}}. \end{cases} \tag{3.19}$$

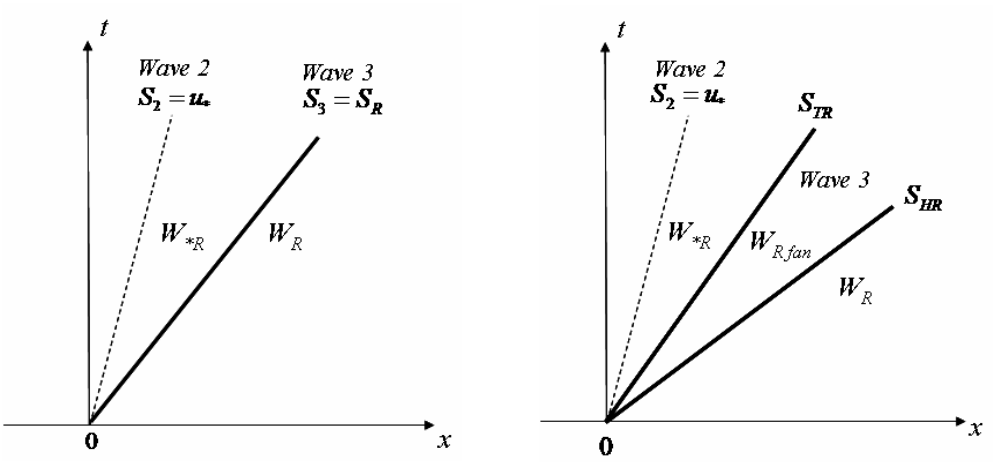

Figure 3.7. Sampling a Solution Point Right of the Contact

In the presence of a rarefaction, primitive variables are determined as

$$\mathbf{W}(x', t) = \begin{cases} \mathbf{W}_{*\mathrm{R}} & \textit{if } u_* \le \dfrac{x'}{t} \le S_{\mathrm{TR}}, \\ \mathbf{W}_{\mathrm{R}\,fan} & \textit{if } S_{\mathrm{TR}} \le \dfrac{x'}{t} \le S_{\mathrm{HR}}, \\ \mathbf{W}_{\mathrm{R}} & \textit{if } \dfrac{x'}{t} \ge S_{\mathrm{HR}}, \end{cases} \tag{3.20}$$

where variables within the fan are calculated (Toro, 1999:136)

$$\mathbf{W}_{\mathrm{R}\,fan}(\mathbf{W}_{\mathrm{R}}, x', t) = \begin{cases} \rho = \rho_{\mathrm{R}} \left[\dfrac{2}{\gamma+1} - \dfrac{\gamma-1}{a_{\mathrm{R}}(\gamma+1)} (u_{\mathrm{R}} - \dfrac{x'}{t}) \right]^{\frac{2}{\gamma-1}}, \\ u = \dfrac{2}{\gamma+1} \left[-a_{\mathrm{R}} + \dfrac{(\gamma-1)}{2} u_{\mathrm{R}} + \dfrac{x'}{t} \right], \\ p = p_{\mathrm{R}} \left[\dfrac{2}{\gamma+1} - \dfrac{\gamma-1}{a_{\mathrm{R}}(\gamma+1)} (u_{\mathrm{R}} - \dfrac{x'}{t}) \right]^{\frac{2\gamma}{\gamma-1}}. \end{cases} \tag{3.21}$$

The entire solution of the Riemann problem is defined.

3.5. Validation of the ERS – The Sod Shock Tube Test

The developed Riemann solver was validated against a classical shock tube problem presented by Sod in 1978. The shock tube is one meter long, and contains a diaphragm, positioned at $x = 0.5$m, which separates two constant initial states

$$\mathbf{W}(x, 0) = \begin{cases} \mathbf{W}_{\mathrm{L}} = (1.000\ \mathrm{kg/m^3}, 0.0\ \mathrm{m/sec}, 1.0\ \mathrm{N/m^2}) & x < 0.5\mathrm{m}, \\ \mathbf{W}_{\mathrm{R}} = (0.125\ \mathrm{kg/m^3}, 0.0\ \mathrm{m/sec}, 0.1\ \mathrm{N/m^2}) & x > 0.5\mathrm{m}. \end{cases}$$

The solution, consisting of a left rarefaction, contact, and right shock wave pattern, develops over the time interval $t = [0.0, 0.25]$ sec. Profiles of primitive variables and internal energy at 10,001 equally-spaced points throughout the shock tube are depicted in Figure 3.8 - Figure 3.11. In addition to the Sod test, four other shock tests were solved using the ERS. The solutions to these tests consisted of combinations of strong shocks and rarefactions (Einfeldt et. al., 1991:273-295; Woodward and Colella, 1984:115-173). Numerical results proved consistent with published data for all tests.

The exact Riemann solver algorithm serves as the basis for subsequent methods which treat a computational domain as a series of local Riemann problems. Furthermore, the solver applied to the Sod shock tube test provides a benchmark for comparing calculations determined by finite volume techniques.

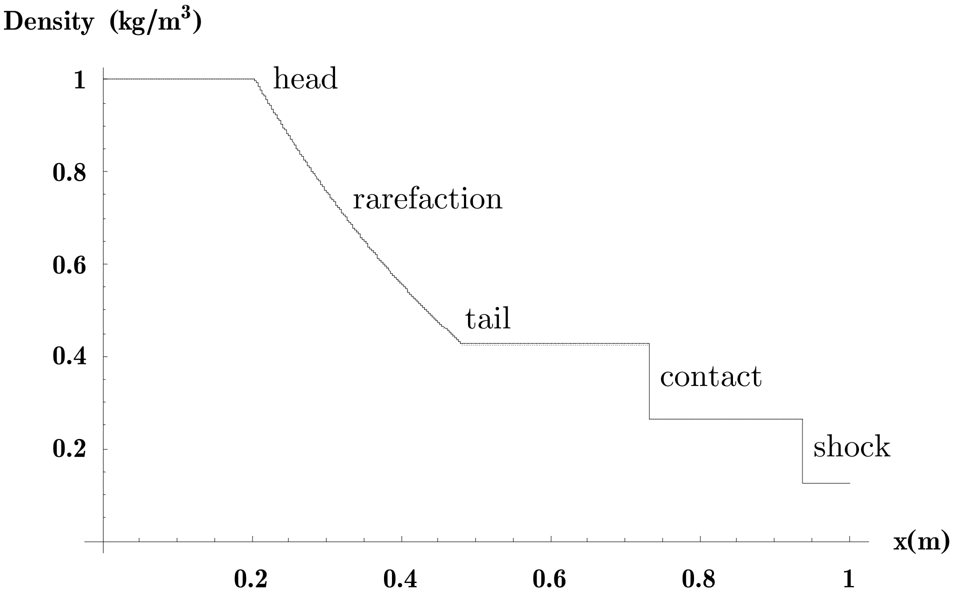

Figure 3.8. Density Profile at $t = 0.25$ sec

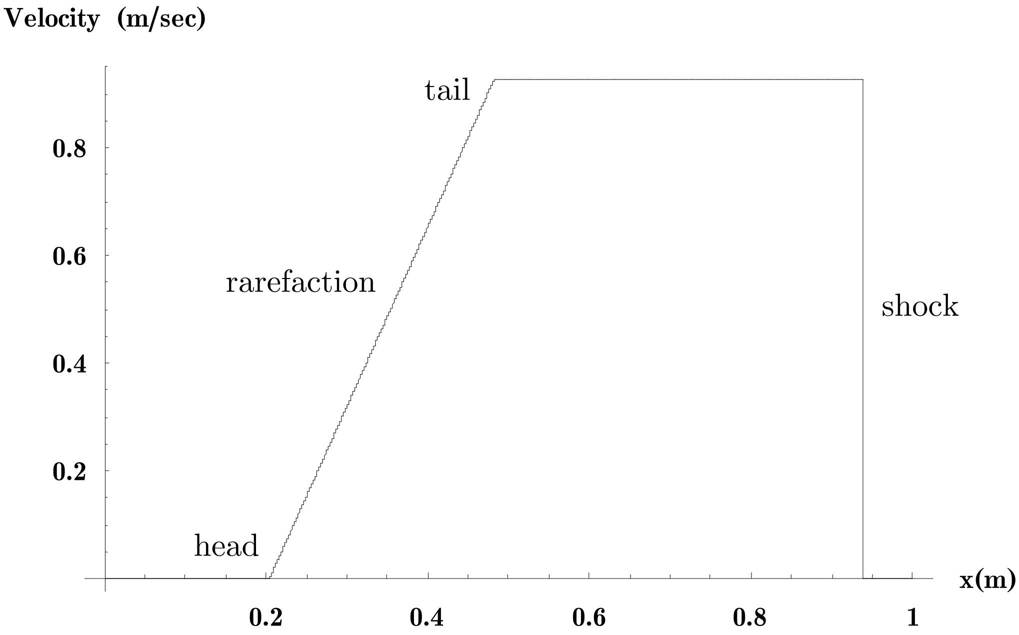

Figure 3.9. Material Velocity Profile at $t = 0.25$ sec

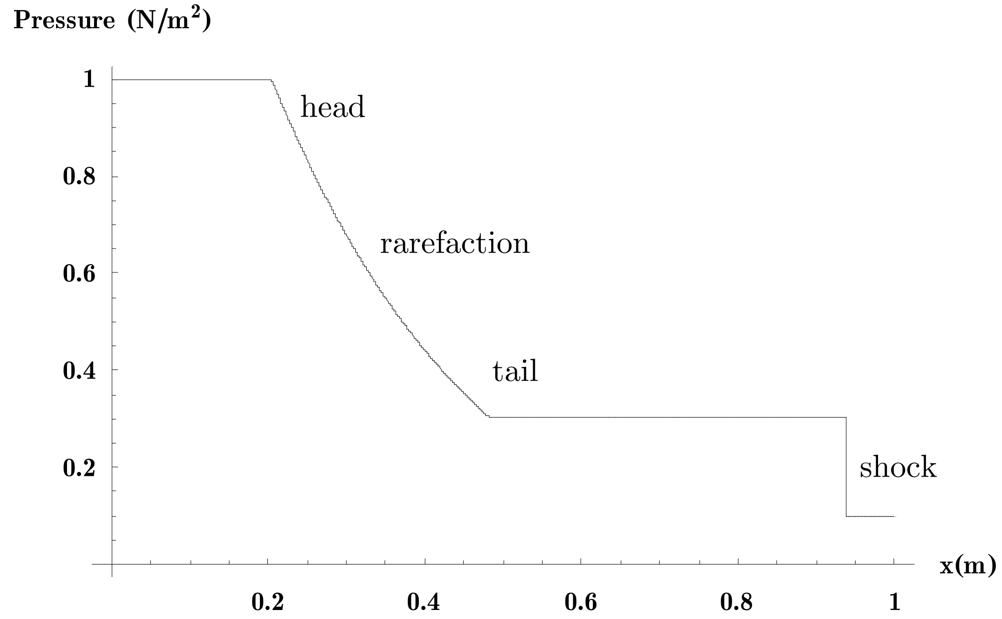

Figure 3.10. Pressure Profile at $t = 0.25$ sec

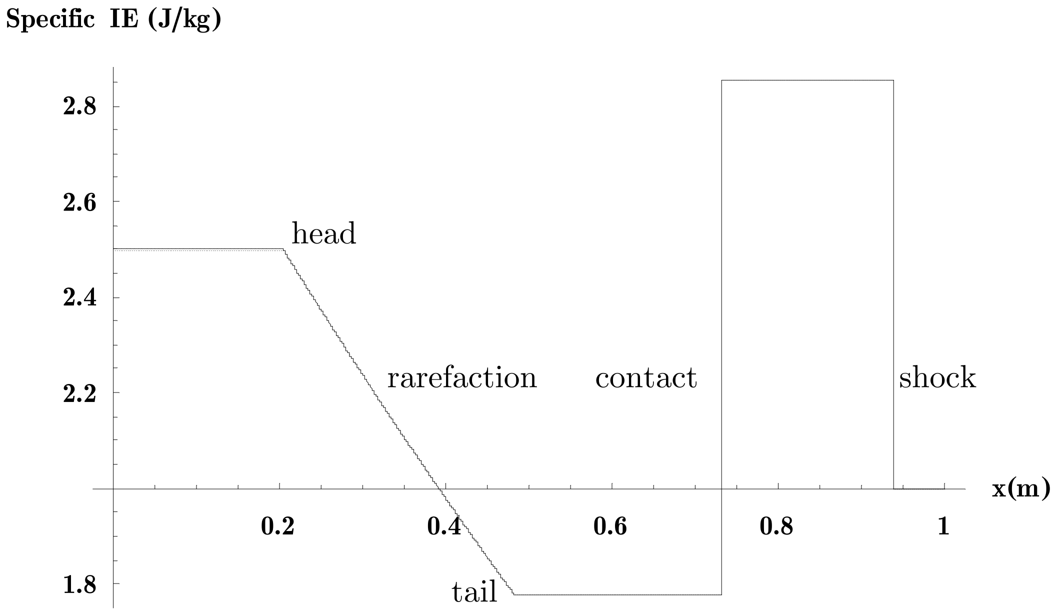

Figure 3.11. Specific Internal Energy Profile at $t = 0.25$ sec

4. Code Implementation in One Dimension

4.1. Overview

A general scheme for non-linear hyperbolic systems of equations is presented in this chapter. Finite volume techniques are introduced and applied to the time-dependent Euler conservation equations in a single dimension. Godunov's first-order upwind conservative method, which employs exact solutions to local Riemann problems in order to calculate numerical intercell fluxes, is described. Improvements to computational efficiency are introduced as approximate Riemann solvers. Second-order extensions of Godunov's method and total variation diminishing (TVD) techniques are implemented to improve solution accuracy. The developments presented allow relaxation of symmetry, which Toro's ERS assumes, in order to obtain solutions to more extensive categories of problems than the ERS permits. The developed computational model is validated against the benchmark shock tube test, as well as a documented experimental shock test.

4.2. Initial Boundary Value Problem (IBVP)

The one-dimensional initial boundary value problem for non-linear systems of hyperbolic conservation laws, assuming uniform flows in the y and z directions is defined as

$$\begin{aligned} &\textit{PDEs :}\ \ \mathbf{U}_t + \mathbf{F}(\mathbf{U})_x = 0, \\ &\textit{ICs :}\ \ \ \ \mathbf{U}(x,0) = \mathbf{U}^{(0)}(x), \\ &\textit{BCs :}\ \ \ \mathbf{U}(0,t) = \mathbf{U}_{\mathrm{L}}(t);\ \mathbf{U}(L,t) = \mathbf{U}_{\mathrm{R}}(t). \end{aligned} \tag{4.1}$$

$\mathbf{U}(x,\ t)$ is a vector of conserved variables; $\mathbf{F}(\mathbf{U})$ is a vector of fluxes; $\mathbf{U}^{(0)}(x)$ is the piecewise constant distribution of initial data at time $t = 0$; [0, L] is the spatial domain and the boundary conditions are represented by boundary functions $\mathbf{U}_{\mathrm{L}}(t)$ and $\mathbf{U}_{\mathrm{R}}(t)$ (Toro, 1999:213). Boundary conditions may be specified as symmetric, or reflective, or transmissive.

4.3. Domain Discretization

Numerical solutions for the IBVP (4.1) require discretization of the spatial and temporal computational domain. Figure 4.1 introduces a discretized x-t mesh convention where the spatial domain, of length L, is partitioned into I computational cells of uniform width

$$\Delta x = \frac{L}{I}. \tag{4.2}$$

Each computational cell is bounded by faces $i-1/2$ and $i+1/2$ located at

$$\begin{aligned} x_{i-1/2} &= (i-1)\Delta x, \\ x_{i+1/2} &= i\Delta x. \end{aligned} \tag{4.3}$$

The center of the i^{th} computational cell, x_i, is determined as

$$x_i = (i - \frac{1}{2})\Delta x. \tag{4.4}$$

Figure 4.1 shows non-uniform time steps which are determined, adaptively, as

$$\Delta t = \frac{C_{cfl}\Delta x}{S^n_{max}}. \tag{4.5}$$

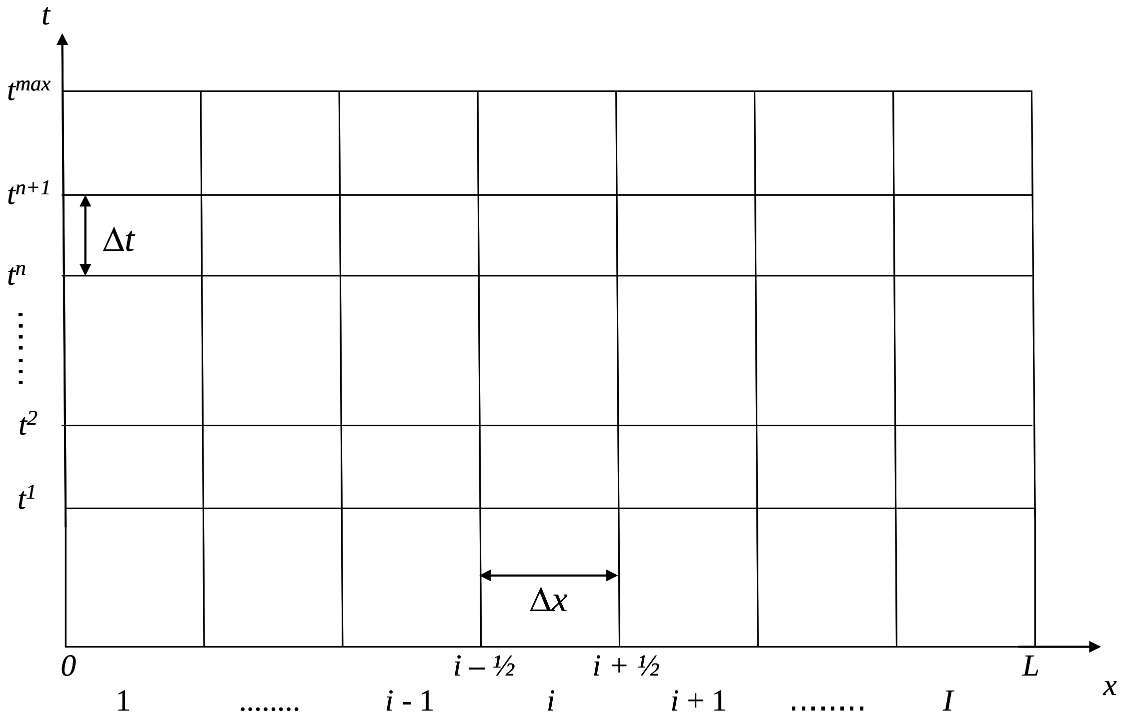

Figure 4.1. Discretized Domain

C_{cfl} is the Courant coefficient satisfying the condition

$$0 < C_{cfl} < 1. \tag{4.6}$$

As C_{cfl} approaches one, the time stepping scheme exhibits maximum efficiency. S^n_{max} is the maximum wave speed present throughout the spatial domain during time level n. For the time-dependent, Euler equations, a reliable approximation for S^n_{max}, which extends to multi-dimensional problems, (Toro, 1999:221) is

$$S^n_{max} = max\left\{\left|u^n_i\right| + a^n_i\right\}. \tag{4.7}$$

The conditions set forth in (4.5) - (4.7) predict no wave present in the solution of all Riemann problems travels a distance greater than Δx during Δt. This prediction correlates directly to solution stability during a time step, and will be further discussed later.

With the x-t domain fully discretized, solutions for (4.1) ensue. Results are the piecewise constant distribution of cell averaged values assigned to computational cells as (Toro, 1999:215)

$$\mathbf{U}(x, t^n) = \mathbf{U}_i^n . \tag{4.8}$$

4.4. Discretization of the Euler Conservation Equations

In order to discretize (4.1) as applied to the Euler conservation equations, discontinuous solutions must be considered. In these cases, the smoothness assumption that leads to the differential form of the conservation equations no longer holds true (Toro, 1999:19). Therefore, development of a finite volume discretized form of (4.1) begins with consideration of the integral form of the equations applied to a control volume $[x_1, x_2] \times [t_1, t_2]$ in the domain of interest. Integrating the system of conservation equations in x-t space and using Green's theorem yields the integral form of the conservation equations

$$\oint \left[\mathbf{U}\, dx - \mathbf{F}(\mathbf{U}) dt \right] = \mathbf{0}, \tag{4.9}$$

where the line integration is performed, counter-clockwise, along the boundary of the domain (Toro, 1999:62). This integral may be expanded as

$$\int_{x_1}^{x_2} \mathbf{U}(x,t_2)dx = \int_{x_1}^{x_2} \mathbf{U}(x,t_1)dx + \int_{t_1}^{t_2} \mathbf{F}(\mathbf{U}(x_1,t))dt - \int_{t_1}^{t_2} \mathbf{F}(\mathbf{U}(x_2,t))dt \ , \qquad (4.10)$$

which yields the conservative, discretized form of the Euler conservation equations (Toro, 1999:217)

$$\mathbf{U}_i^{n+1} = \mathbf{U}_i^n + \frac{\Delta t}{\Delta x}[\mathbf{F}_{i-1/2} - \mathbf{F}_{i+1/2}]. \qquad (4.11)$$

Simply stated, (4.11) indicates the solution $\mathbf{U}_i^{n+1}$ is determined by $\mathbf{U}_i^n$ and the net flux through a cell where $\mathbf{F}_{i-1/2}$ represents the conserved variable flux entering the cell through face $i-1/2$ and $\mathbf{F}_{i+1/2}$ is the flux exiting the cell through face $i+1/2$. These numerical fluxes are determined via equation (2.6). The solutions for primitive variables at each cell face, required to solve (2.6), are evaluated by solving Riemann problems at the faces. Godunov's scheme provides a method to determine all components required for solutions of (4.11) for a computational domain.

4.5. The Godunov Scheme

Godunov's first-order upwind method is a conservative method of the form (4.11) where intercell numerical fluxes are computed using solutions of local Riemann problems. Spatial discretization for a given time step is depicted in Figure 4.2.

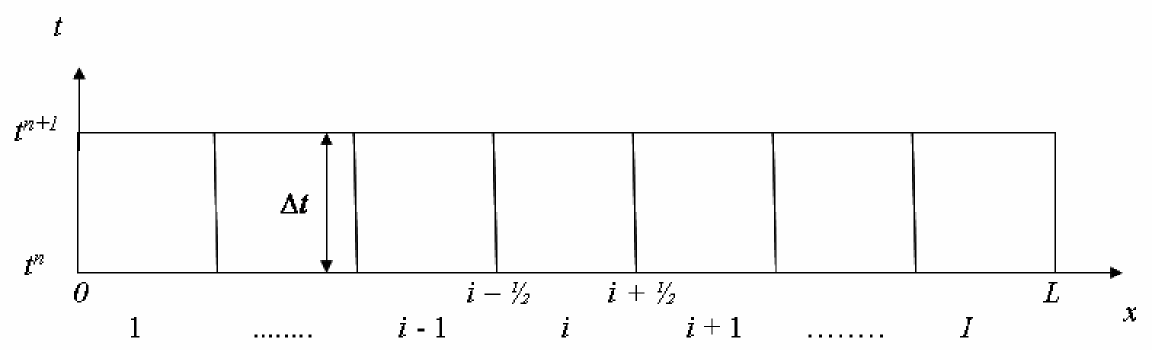

Figure 4.2. Domain Discretization for a Single Time Step

Note that each pair of cells provides information to solve the RP, in primitive variable form, at the shared cell face $i+1/2$ during time step Δt such that

$$\begin{aligned} &\mathbf{W}_t + \mathbf{F}(\mathbf{W})_x = \mathbf{0}, \\ &\mathbf{W}(x,t^n) = \mathbf{W}_i^n = \begin{cases} \mathbf{W}_i & x < 0 \\ \mathbf{W}_{i+1} & x > 0. \end{cases} \end{aligned} \tag{4.12}$$

Therefore, exact solutions for (4.12) at each cell face provide the requisite information to determine conserved variable fluxes, via equation (2.6). These fluxes, coupled with cell conserved variable values at the beginning of a time step, $\mathbf{U}_i^n$, and a specified time step determined by (4.5) facilitate solutions for cell conserved variables $\mathbf{U}_i^{n+1}$ at the end of a time step. Finally, these updated cell conserved variables serve as initial conditions for the RPs during the subsequent time step.

Several aspects of Godunov's scheme require special consideration. Specifically, in order to solve the RPs at $x=0$ and $x=\mathrm{L}$, and update solutions in cells 1 and M, computational cells must exist to the left of $x=0$ and to the right of $x=\mathrm{L}$, respectively. Additionally, determination of a time step Δt which maximizes computational efficiency and stability is significant. Finally, calculating primitive variables and, hence, numerical fluxes through cell faces requires a modification to the ERS sampling procedure.

4.6. Special Considerations

4.6.1. Phantom Cells

The imposition of phantom cells ensures that solutions at the computational domain boundaries are consistent with conditions defined by the physical model. When modeling shocks, two types of boundaries are considered: reflective, or symmetric, and transmissive.

If the boundary located at $x=\mathrm{L}$ represents, physically, a fixed, reflective, impermeable surface, then the physical border is correctly modeled by a fictitious or phantom state $\boldsymbol{W}_{I+1}^{n}$ that is defined from the known computational state $\boldsymbol{W}_{I}^{n}$ such that

$$\rho_{I+1}^{n}=\rho_{I}^{n} \;\;,\;\; u_{I+1}^{n}=-u_{I}^{n} \;\;,\;\; p_{I+1}^{n}=p_{I}^{n}. \tag{4.13}$$

Similarly, a physically symmetric boundary location at $x=0$ requires

$$\rho_{0}^{n}=\rho_{1}^{n} \;\;,\;\; u_{0}^{n}=-u_{1}^{n} \;\;,\;\; p_{0}^{n}=p_{1}^{n}. \tag{4.14}$$

Transmissive conditions attempt to numerically reproduce boundaries that allow the physical passage of waves without any effect on them. For this case, the primitive variables in phantom cells at $x=\mathrm{L}$ and $x=0$ are defined as

$$\rho_{I+1}^{n}=\rho_{I}^{n} \;\;,\;\; u_{I+1}^{n}=u_{I}^{n} \;\;,\;\; p_{I+1}^{n}=p_{I}^{n}, \tag{4.15}$$

and

$$\rho_0^n = \rho_1^n \ , \ u_0^n = u_1^n \ , \ p_0^n = p_1^n . \tag{4.16}$$

Although transmissive boundaries work well in a single dimension, attempts to model their effects in multi-dimensional problems produces false reflections, and is an area of significant ongoing research (Toro, 1999:224).

4.6.2. Time Step Stability

Recall that a stable time step is approximated from the conditions defined in (4.5) - (4.7). Now consider the solutions to the Riemann problems at cell faces $x_{i+1/2}$ and $x_{i+3/2}$ as depicted in Figure 4.3. Observe the left traveling shock, resulting from the solution of the RP at $x_{i+3/2}$, travels rapidly to the left and reaches the boundary located at $x_{i+1/2}$ before the completion of time step Δt. This shock effectively interferes with the solution of the RP at $x_{i+1/2}$ and results in an erroneous flux calculation that propagates outward toward other cells. As incorrect computations are advanced forward in time, errors are compounded introducing numerical instabilities. To remedy this problem, the time step is shortened to $\Delta t'$ and interference between adjacent RPs is avoided.

Time steps are easily shortened by modifying the value of the CFL coefficient. Recall the maximum wave speed is approximated by cell values of material velocity and speed of sound. For shock tests where stationary states initially exist $(u = 0)$ the maximum wave wave speed is dominated by the speed

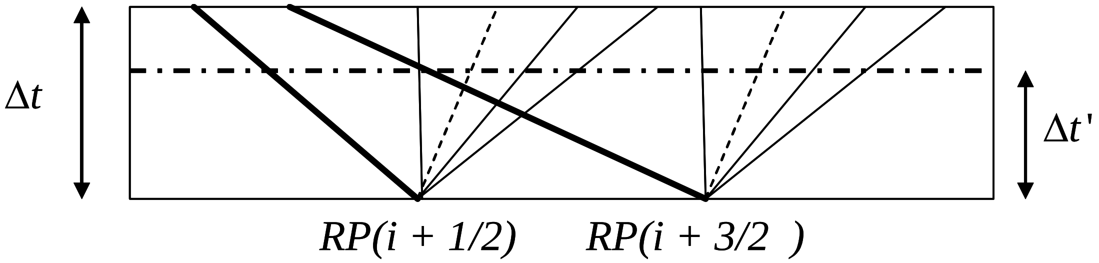

Figure 4.3. Wave Patterns in Adjacent Riemann Problems

of sound, and is often underestimated. The result is a time step that is too large which, potentially, introduces instabilities early in the computations. In order to maximize stability and computational efficiency, Toro recommends $C_{cfl} = 0.2$ for the first five time steps, and $C_{cfl} = 0.9$ thereafter.

4.6.3. Sampling

Chapter 3 presented the complete exact solution to a general Riemann problem for the Euler equations. Recall that the sampling procedure requires a coordinate transformation from the physical domain of the shock tube, x, to the computational domain, x', of the RP. The solution for primitive variables at a given point within the shock tube is then determined by comparing x'/t to the wave speeds generated by the RP.

For Godunov's scheme, sampling is performed at the cell face, only, for the special value $x'/t = 0$. Recall the ERS determined that $x'/t < u_*$ indicated the sample point was located left of the contact wave. For Godunov's method, this is analogous to $u_* > 0$. Similarly, $u_* < 0$ indicates the sample point, or intercell boundary, is located right of the contact when applying Godunov's scheme.

Finally, each of the shock and rarefaction wave patterns analyzed during ERS sampling must be taken into account by Godunov's method.

Godunov's scheme may be summarized as follows. Following application of boundary conditions, via phantom cells, a stable time step is approximated. At each cell face, a Riemann problem is solved, exactly, in order to determine primitive variables at the face. The RP solutions allow determination of conserved variable fluxes through each face from equation (2.6). Finally, conserved variables in each cell are updated by (4.11) and primitive variables are determined by equation (2.4). The scheme continues, forward in time, until the desired solution time is achieved.

4.7. Numerical Results of Godunov's Method

Here the performance of Godunov's method is analyzed against the benchmark shock tube test from Chapter 3, consisting of a left rarefaction, contact, and right shock. The results were determined using a spatial domain discretized with I = 200 computational cells. Boundary conditions were set as transmissive; Toro's method for CFL coefficient selection was applied. Figure 4.4 shows a density profile at $t = 0.25$ sec following 125 time steps.

Solutions are smeared at the shock and contact discontinuities, as well as at the head and tail of the rarefaction, which is a common feature of first-order methods. Note that the shock front is smeared over four cells, while the contact surface is distributed over 27 cells. In general, contact waves are more

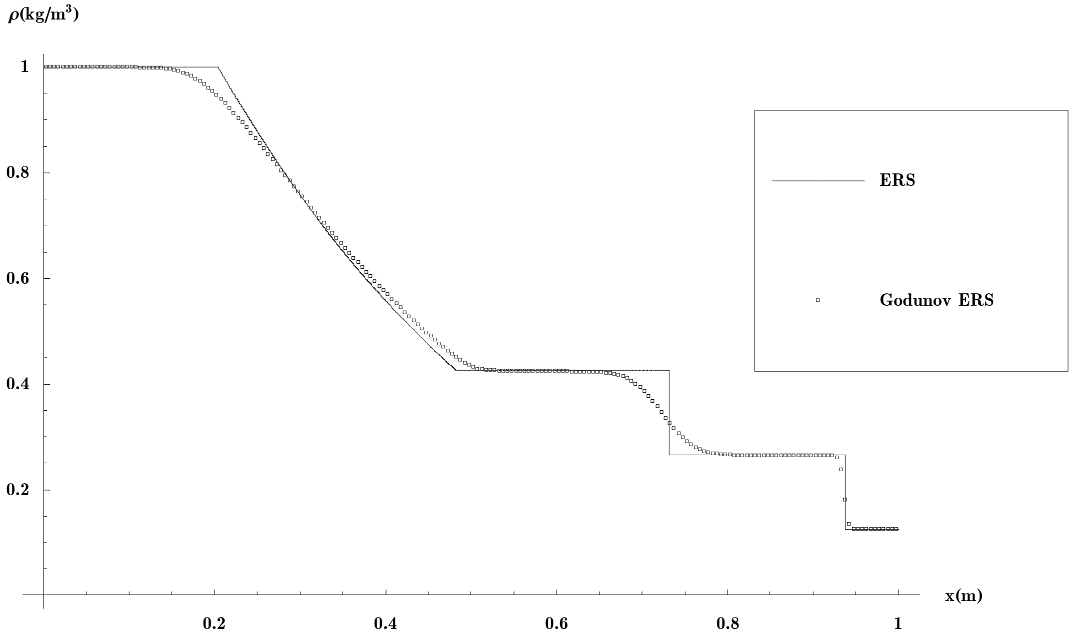

Figure 4.4. ERS vs. Godunov Density Profile at t = 0.25 sec

difficult to resolve than shocks due to the behavior of the characteristics. Recall the characteristics on either side of a contact run parallel to the discontinuity, while shock characteristics run into the shock. This compression mechanism effectively enhances numerical shock resolution. Lastly, the rarefaction wave, which is a smooth flow feature, exhibits smearing near the head and tail, where a discontinuity in the derivative exists (Toro, 1999:227).

It is expected that resolution would improve at each smearing location as the coarse mesh of 200 cells is refined. In fact, increasing the number of computational cells by a factor of five, from 200 to 1000, achieves improved resolution at solution and derivative discontinuities, as depicted in Figure 4.5.

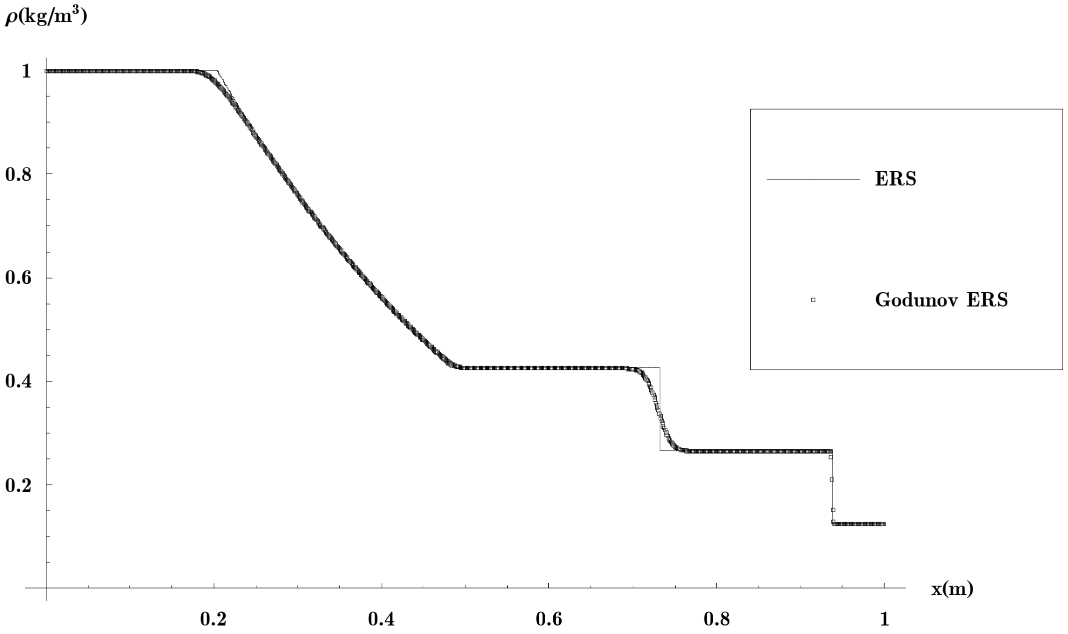

Figure 4.5. ERS vs. Godunov Density Profile (1000 cells) at t = 0.25 sec

Here, the shock front remains smeared over four cells, while the contact discontinuity is resolved over 64 cells. Because the spatial mesh refinement did not increase smearing of the contact surface by the same factor of five, resolution of the associated numerical solutions is improved.

Godunov's method, used in conjunction with an exact Riemann solver, is shown to accurately predict the locations and speeds of each wave. This feature of the scheme is important when modeling shock propagation. Furthermore, the method guarantees monotonic solutions (Toro, 1999:226) near discontinuities, which will prove significant when implementing second-order methods. Finally, practical computations involving Godunov's method require solutions to billions of Riemann problems, making the iterative ERS solution process the most demanding task in the numerical method. In the next section, improvements in computational efficiency, to include solution approximations, are examined.

4.8. Adaptive Riemann Solvers

The computational effort required by the iterative exact Riemann solver may not always prove justifiable. For this reason, several non-iterative approximate Riemann solvers have been developed in recent decades. These improved solution algorithms are based on Godunov's scheme, and offer the benefit of improved efficiency without sacrificing accuracy. Riemann problem solutions may be estimated by one of two methods: numerical flux approximations or state approximations. The latter form the basis for modern Godunov-type methods and are examined here.

Recall the exact Riemann solver requires finding the root of Toro's pressure equation in order to ultimately determine values for primitive variables in the star region. Toro presents three approximations, based on known left and right states, and an assumption of wave patterns in the RP, that predict these same variables with equal accuracy and greater efficiency than the exact techniques. Furthermore, Toro includes a set of conditions that apply known state variables to adaptively select the most favorable value of the determined approximations.

Toro's techniques are easily implemented because two of the three approximate Riemann solvers are based upon the exact Riemann solver.

Additionally, adaptive selection of the most favorable approximation applies the same logic used to select the initial pressure guess for Newton's method in the ERS.

Toro refers to the three approximate Riemann solvers as the primitive variable Riemann solver (PVRS), two-rarefaction Riemann solver (TRRS) and two-shock Riemann solver (TSRS). The logic sequence for selecting an approximate solver (Toro, 1999:306) is included in Figure 4.6, followed by governing equations for each solver.

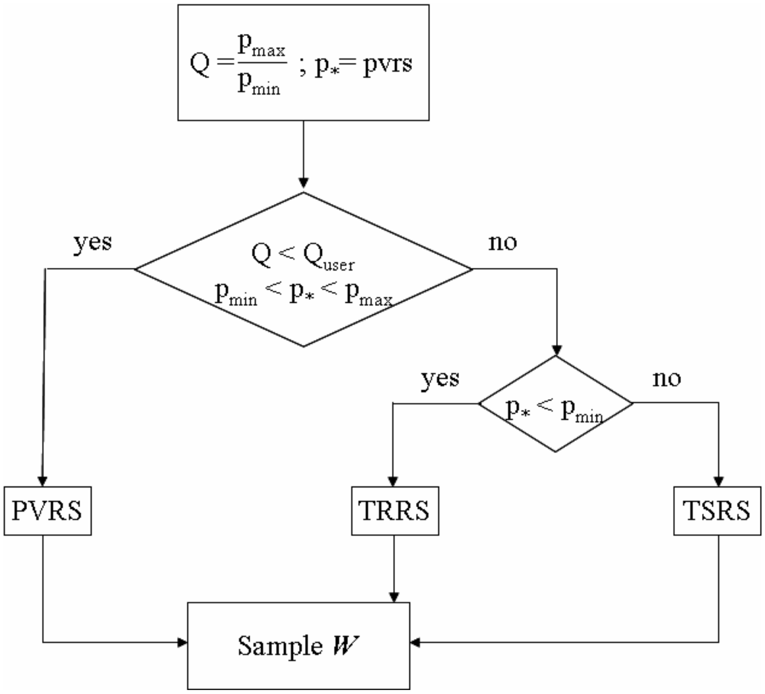

Figure 4.6. Logic Sequence for Adaptive Noniterative Riemann Solver

The PVRS relies on the assumption that smooth flows exist in the region of interest. This assumption yields a linear, hyperbolic system of equations which is solved, exactly, to provide relationships for primitive variables in the star region as

$$\mathbf{W}_{PVRS}(\mathbf{W}_\mathrm{L},\mathbf{W}_\mathrm{R})=\begin{cases} p_* = \dfrac{1}{2}(p_\mathrm{L}+p_\mathrm{R})+\dfrac{1}{8}[(u_\mathrm{L}-u_\mathrm{R})(\rho_\mathrm{L}+\rho_\mathrm{R})(a_\mathrm{L}+a_\mathrm{R})], \\ u_* = \dfrac{1}{2}(u_\mathrm{L}+u_\mathrm{R})+2\left[\dfrac{(p_\mathrm{L}-p_\mathrm{R})}{(\rho_\mathrm{L}+\rho_\mathrm{R})(a_\mathrm{L}+a_\mathrm{R})}\right], \\ \rho_{*\mathrm{L}} = \rho_\mathrm{L}+\dfrac{(u_\mathrm{L}-u_*)(\rho_\mathrm{L}+\rho_\mathrm{R})}{(a_\mathrm{L}+a_\mathrm{R})}, \\ \rho_{*R} = \rho_R+\dfrac{(u_*-u_\mathrm{R})(\rho_\mathrm{L}+\rho_\mathrm{R})}{(a_\mathrm{L}+a_\mathrm{R})}. \end{cases} \tag{4.17}$$

Recall the exact Riemann solver pressure function

$$f_L(p_*,\mathbf{W}_\mathrm{L})+f_R(p_*,\mathbf{W}_\mathrm{R})+u_\mathrm{R}-u_\mathrm{L}=0, \tag{4.18}$$

where the left and right functions are based on the classification of the outer waves in the RP as

$$f_\xi(p_*,\mathbf{W}_\xi)=\begin{cases} (p_* - p_\xi)\left(\dfrac{2}{\rho_\xi(p_*(\gamma+1)+\rho_\xi(\gamma-1))}\right)^{\frac{1}{2}} & \textit{if} \quad p_* > p_\xi \ (\textit{shock}), \\ \dfrac{2a_\xi}{\gamma-1}\left[\left(\dfrac{p_*}{p_\xi}\right)^{\frac{\gamma-1}{2\gamma}}-1\right] & \textit{if} \quad p_* \le p_\xi \ (\textit{rarefaction}). \end{cases} \tag{4.19}$$

The TRRS assumes both outer waves are rarefactions and substitutes the appropriate relationships from (4.19) into (4.18). The resulting closed-form solutions for primitive variables in the star region (Toro, 1999:301) are calculated as

$$W_{TRRS}(\mathbf{W}_{\mathrm{L}},\mathbf{W}_{\mathrm{R}}) = \begin{cases} p_* = \left[\dfrac{a_{\mathrm{L}} + a_{\mathrm{R}} - \dfrac{\gamma-1}{2\gamma}(u_{\mathrm{L}} - u_{\mathrm{R}})}{\dfrac{a_{\mathrm{L}}}{p_{\mathrm{L}}^{(\frac{\gamma-1}{2\gamma})}} + \dfrac{a_{\mathrm{R}}}{p_{\mathrm{R}}^{(\frac{\gamma-1}{2\gamma})}}}\right]^{\frac{2\gamma}{\gamma-1}}, \\ u_* = \dfrac{1}{2}(u_{\mathrm{L}} + u_{\mathrm{R}}) + \dfrac{1}{2}[f_{\mathrm{R}}(p_*) - f_{\mathrm{L}}(p_*)], \\ \rho_{*\mathrm{L}} = \rho_{\mathrm{L}}\left(\dfrac{p_*}{p_{\mathrm{L}}}\right)^{\frac{1}{\gamma}}, \\ \rho_{*R} = \rho_R\left(\dfrac{p_*}{p_R}\right)^{\frac{1}{\gamma}}. \end{cases} \tag{4.20}$$

Similarly, the TSRS classifies both outer waves as shocks. Unfortunately, this approximation does not lead to a closed form solution. Resulting quadratic equations lead to non-uniqueness of solutions and, in the case of complex roots, non-existence of solutions. An acceptable alternative is to first estimate pressure as p_{pvrs} and then apply the two-shock assumption to solve the pressure function. The resulting equations are

$$W_{TSRS}(\mathbf{W}_{\mathrm{L}},\mathbf{W}_{\mathrm{R}},p_0) = \begin{cases} p_* = \dfrac{g_{\mathrm{L}}(p_0)p_{\mathrm{L}} + g_{\mathrm{R}}(p_0)p_{\mathrm{R}} - (u_{\mathrm{R}} - u_{\mathrm{L}})}{g_{\mathrm{L}}(p_0) + g_{\mathrm{R}}(p_0)}, \\ u_* = \dfrac{1}{2}(u_{\mathrm{L}} + u_{\mathrm{R}}) + \dfrac{1}{2}[(p_* - p_{\mathrm{R}})g_{\mathrm{R}}(p_0) - (p_* - p_{\mathrm{L}})g_{\mathrm{L}}(p_0)], \\ \rho_{*\mathrm{L}} = \rho_{\mathrm{L}}\left[\dfrac{\dfrac{p_*}{p_{\mathrm{L}}} + \dfrac{(\gamma-1)}{(\gamma+1)}}{\dfrac{(\gamma-1)}{(\gamma+1)}\dfrac{p_*}{p_{\mathrm{L}}} + 1}\right], \\ \rho_{*\mathrm{R}} = \rho_{\mathrm{R}}\left[\dfrac{\dfrac{p_*}{p_{\mathrm{R}}} + \dfrac{(\gamma-1)}{(\gamma+1)}}{\dfrac{(\gamma-1)}{(\gamma+1)}\dfrac{p_*}{p_{\mathrm{R}}} + 1}\right], \end{cases} \tag{4.21}$$

where

$$p_0 = \max(0, p_{PVRS}) \tag{4.22}$$

and

$$g_\xi(p_0) = \left[\frac{2}{\rho_\xi\left[(\gamma+1)\,p_0 + (\gamma-1)\,p_\xi\right]}\right]^{\frac{1}{2}}. \tag{4.23}$$

The adaptive techniques were implemented in the computational model and applied to the benchmark shock tube test. Parameters discussed in section 4.7 were maintained. A comparison of the test results is shown in Figure 4.7.

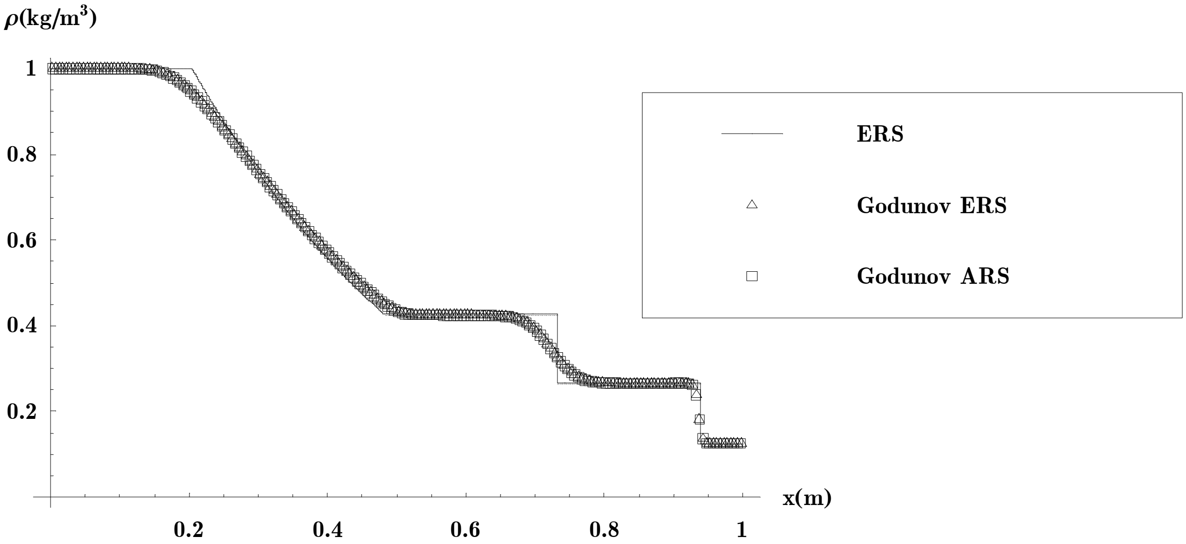

Figure 4.7. Comparison of Godunov's Method Using ERS and ARS

While the results generated by the exact and approximate techniques appear graphically identical, the computational costs differ significantly. Specifically, calculations executed with the approximate solver, for all five shock tests presented by Toro, ran, on average, nearly 36% faster than exact computations. Based on this observation, I conclude that the approximate solver is best suited for all subsequent calculations. Finally, an accurate and efficient first-order method is established and second-order accuracy is examined next.

4.9. E.F. Toro's Weighted Average Flux (WAF) Method

Here a second-order extension to Godunov's method is explored. Flux calculations in Godunov's first-order scheme require solutions to Riemann problems along cell faces only. The weighted average flux method analyzes the full structure of the RP in order to determine the total flux through a cell face. Toro presents two versions of his WAF method. The first scheme determines an integral average of the flux across the full solution of a local RP. The second version computes a weighted average state of primitive variables across the local RP and applies these states to determine WAF (Toro, 1999:492). The latter version requires fewer flux calculations than the former, and is implemented here due to its computational efficiency.

Weighted average flux is defined as (Toro, 1999:429)

$$\mathbf{F}_{i+1/2} \equiv \frac{1}{\Delta x} \int_{-\Delta x/2}^{\Delta x/2} \mathbf{F}(\mathbf{U}_{i+1/2}(x, \frac{\Delta t}{2}))\, dx \,. \qquad (4.24)$$

As applied to the weighted average state (WAS) version of flux, (4.24) may be rewritten

$$\mathbf{F}_{i+1/2} = \frac{1}{\Delta x} \int_{-\Delta x/2}^{\Delta x/2} \mathbf{F}(\overline{\mathbf{W}}_{i+1/2}(x, \frac{\Delta t}{2}))\, dx \qquad (4.25)$$

where the WAS of primitive variables across a local RP is expressed

$$\overline{\mathbf{W}}_{i+1/2} \equiv \frac{1}{\Delta x} \int_{-\Delta x/2}^{\Delta x/2} \mathbf{W}_{i+1/2}(x, \frac{\Delta t}{2}))\,dx\,. \tag{4.26}$$

Figure 4.8 depicts the general wave structure of a local Riemann problem with N waves, where the flux weights, β_k, for $k = 1, \ldots, N+1$ are normalized lengths of segments $A_{k-1}A_k$ such that $\beta_k = |A_{k-1}A_k| / \Delta x$.

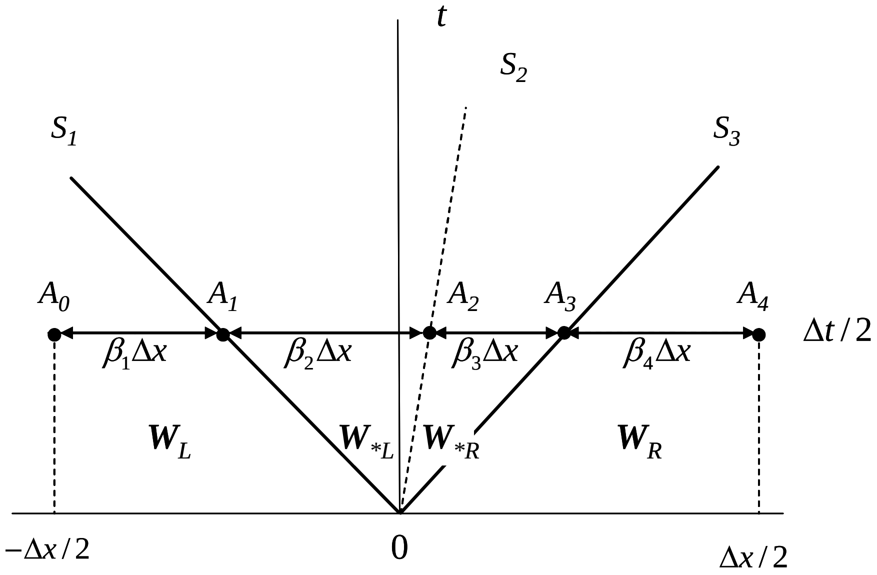

Figure 4.8. General Wave Structure of a Local Riemann Problem

These weights can be expressed, in terms of the wave speeds, as

$$\left.\begin{aligned} \beta_k &= \frac{1}{2}(c_k - c_{k-1}), \\ c_k &= \frac{\Delta t S_k}{\Delta x}, \quad c_0 = -1, \quad c_{N+1} = 1. \end{aligned}\right\} \tag{4.27}$$

Here c_k is the local courant number for wave k moving with speed S_k and represents the fraction of the cell width that the k^{th} wave traverses during a time step Δt. In expanded form, the weights are expressed as

$$\beta_1 = \frac{1}{2}(1 + c_1), \quad \beta_2 = \frac{1}{2}(c_2 - c_1), \quad \beta_3 = \frac{1}{2}(c_3 - c_2), \quad \beta_4 = \frac{1}{2}(1 - c_3). \qquad (4.28)$$

For the wave structure of Figure 4.8, the WAS integral (4.26) becomes

$$\overline{\mathbf{W}}_{i+1/2} = \sum_{k=1}^{N+1} \beta_k \, \mathbf{W}_{i+1/2}^{k} \qquad (4.29)$$

where the corresponding states are defined as

$$\mathbf{W}^{(1)} = \mathbf{W}_L \;, \quad \mathbf{W}^{(2)} = \mathbf{W}_{*L} \;, \quad \mathbf{W}^{(3)} = \mathbf{W}_{*R} \;, \quad \mathbf{W}^{(4)} = \mathbf{W}_R \,, \qquad (4.30)$$

and

$$\sum_{k=1}^{N+1} \beta_k = 1 \,. \qquad (4.31)$$

The weighted average state of each primitive variable is now fully defined. Weighted average flux is determined merely by applying equation (2.6) to the WAS variables.

To demonstrate the second-order extension of Godunov's method, the Sod shock test was revisited. Parameters discussed in section 4.7 were maintained. A comparison of test results is shown in Figure 4.9. Inspection of the figure indicates improved resolution at discontinuities over Gounov's first-order method. Specifically, smearing at the contact discontinuity experienced a reduction from

27 cells to 22 cells. However, the WAF method introduced spurious oscillations at each discontinuity, sometimes called Gibb's phenomena, (Toro, 1999: 445) which are common side effects of second order-methods. Analysis of the WAF method and Figure 4.8 provides an explanation of the fluctuations.

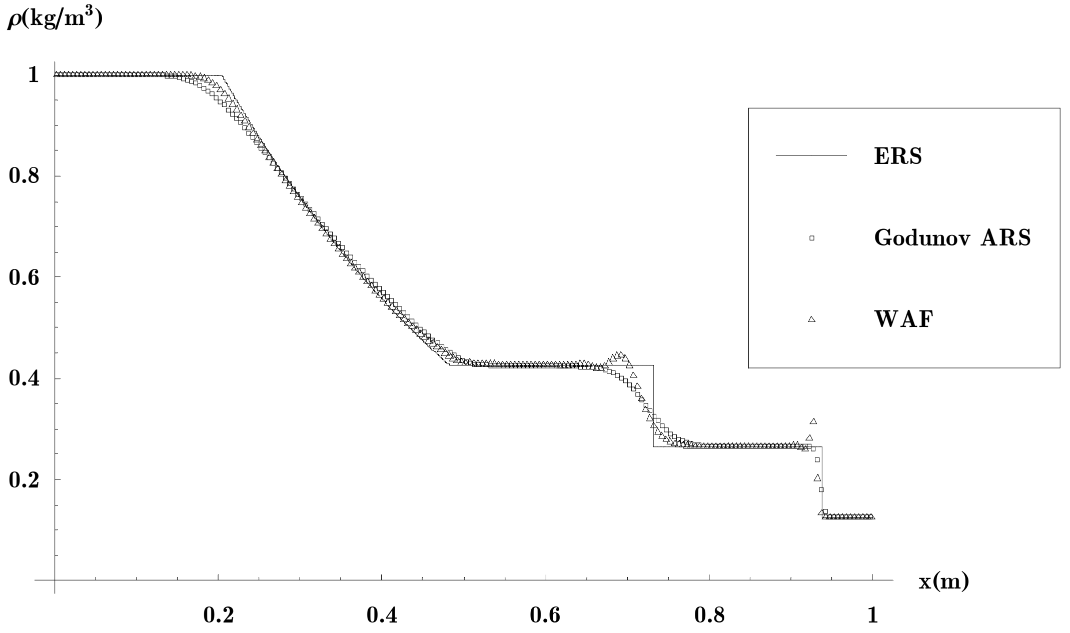

Figure 4.9. WAF Method Density Profile at $t = 0.25$ sec

Recall that Godunov's first-order method determines flux along the cell face, only. Inspection of Figure 4.8 shows, whether $S_2 > 0$ or $S_2 < 0$, that the cell face in the local RP always lies in the upwind portion of the star region. With regard to solutions, upwind flux contributions correlate to stability while downwind contributions facilitate increased accuracy. Therefore, because Godunov's first-order flux calculations contain only an upwind flux contribution, stable solutions, which may be refined for accuracy, are expected. The WAF method introduces these refinements in terms of downwind flux contributions. Note from Figure 4.8 that when $S_2 > 0$ the WAF contribution in the star region consists of the upwind flux with weight β_2, and the downwind flux with weight β_3. For the case $S_2 < 0$, the upwind flux weight in the star region is β_3 while the downwind flux weight is β_2. In both situations, the upwind flux contribution is larger than the downwind contribution and the WAF method is, therefore, upwind biased (Toro, 1999:418). This fact indicates the WAF method maintains the stability of its first order predecessor, but benefits from increased accuracy due to downwind contributions. Unfortunately, these downwind contributions introduce oscillations in discontinuous regions where steep gradients exist. E.F. Toro's limited weighted average flux method uses adaptive, total variation diminishing techniques that effectively ameliorate these oscillations while preserving stability and accuracy.

4.10. E.F. Toro's Limited Weighted Average Flux (LWAF) Method

Total variation diminishing (TVD) schemes are intimately linked to traditional artificial viscosity methods as both techniques attempt to eliminate or control false fluctuations near high gradients. Whereas artificial viscosity schemes introduce oscillation reduction mechanisms explicitly, moderation is inherent in TVD methods.

Given a function $u = u(x,t)$, the total variation of the function at a fixed time $t = t^n$ is denoted $TV(u(t))$. If $u^n = \{u_i^n\}$ is a mesh function, then the total variation of u^n is defined as (Toro, 1999:448)

$$TV(u^n) \equiv \sum_{i=1}^{I} \left| u_{i+1}^n - u_i^n \right|. \tag{4.32}$$

A scheme is said to be TVD if

$$TV(u^{n+1}) \leq TV(u^n), \quad \forall n. \tag{4.33}$$

Finally, the above definitions produce the consequence

$$TV(u^n) \leq TV(u^{n-1}) \leq \ldots \leq TV(u^0). \tag{4.34}$$

Two important characteristics of TVD methods are convergence of solutions and preservation of monotonicity. The benefit of the former is obvious. As for the latter, schemes that preserve monotonic behavior of solutions predict when data $\{u_i^n\}$ is monotonic, the solution set $\{u_i^{n+1}\}$ is monotone in the same manner. Explicitly, if $\{u_i^n\}$ is monotonic increasing so is $\{u_i^{n+1}\}$, and if $\{u_i^n\}$ is monotonic decreasing so is $\{u_i^{n+1}\}$. Because Godunov's first-order method guarantees monotonic solutions near discontinuities, methods that are TVD must preserve this behavior in the presence of strong flows.

In order to limit downwind flux contributions and ensure monotonic behavior near discontinuities, Toro presents four weight limiter functions that effectively regulate flux weights within downwind regions of local Riemann problems. These weight limiter functions, $\phi(r,|c|)$, are derived directly from corresponding flux limiter functions $\psi(r)$ and are related as (Toro, 1999:499)

$$\phi(r,|c|) = 1-(1-|c|)\psi(r)sign(c)\,. \tag{4.35}$$

Here, c is the local courant number given by equation (4.27) and r represents a flow parameter that compares upwind and local density gradients as

$$r = \frac{\Delta\rho_{upw}}{\Delta\rho_{loc}}\,. \tag{4.36}$$

These equations represent scalar relationships applied to a single wave. In practice, solutions of the Euler conservation equations in a single dimension produce three waves resulting from the three conservation laws. Therefore, (4.35) and (4.36) are, in fact, applied across each wave in the solution of the Riemann problem.

Before introducing the governing equations associated with flux limiters, an illustrative examination of flow parameter calculation is presented in Figure 4.10. For each case, the local density gradient at the $i+1/2$ boundary across the k^{th} wave is calculated

$$\Delta\rho_{i+1/2,k} = \rho_{i+1/2,k+1} - \rho_{i+1/2,k}\,. \tag{4.37}$$

For the case where $c_{i+1/2,k} > 0$, the upwind location lies left of the local position and the upwind density gradient is determined at the $i-1/2$ boundary across the k^{th} wave as

$$\Delta\rho_{i-1/2,k} = \rho_{i-1/2,k+1} - \rho_{i-1/2,k} \,. \tag{4.38}$$

Conversely, when $c_{i+1/2,k} < 0$, the upwind site lies right of the local location and the upwind density gradient is calculated at the $i + 3/2$ boundary across the k^{th} wave as

$$\Delta\rho_{i+3/2,k} = \rho_{i+3/2,k+1} - \rho_{i+3/2,k} \,. \tag{4.39}$$

Finally, relationships (4.36) - (4.39) can be conveniently summarized by the equation

$$r_{i+1/2,k} = \frac{\Delta\rho_{i+1/2-(Sign(c)),k}}{\Delta\rho_{i+1/2,k}} \,. \tag{4.40}$$

Determination of the flow parameter introduces a side effect of the LWAF method that requires special consideration. For the case where $c_{i+1/2,k} > 0$ and the local boundary $i + 1/2$ lies at the left edge of the physical domain at $x = 0$, the upwind density gradient across boundary i -- 1/2 requires solution of a Riemann problem via phantom cells 0 and -1. Although phantom cell 0 exists,

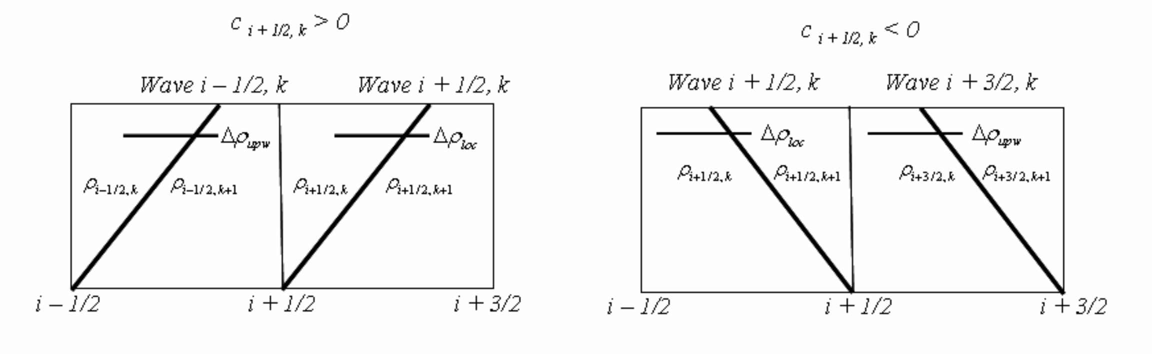

Figure 4.10. Determination of Flow Parameter

cell -1 must be added. Similarly, when $c_{i+1/2,k} < 0$ and the local boundary at $i + 1/2$ lies at the right edge of the physical domain at $x =$ L, the upwind density gradient across boundary $i + 3/2$ requires solution of a Riemann problem using phantom cells I+1 and I+2. Here, phantom cell I+2 is added.

To correctly model physically reflective or symmetric boundary conditions at $x = 0$ and $x =$ L these added phantom cells are defined from known computational states as (Toro, 1999:491)

$$\left.\begin{array}{l} \rho_{-1}^n = \rho_2^n \ \ , \ u_{-1}^n = -u_2^n \ \ , \ \ p_{-1}^n = p_2^n \\ \rho_{I+2}^n = \rho_{I-1}^n \ \ , \ u_{I+2}^n = -u_{I-1}^n \ \ , \ \ p_{I+2}^n = p_{I-1}^n \end{array}\right\} . \tag{4.41}$$

Likewise, transmissive boundaries are given by

$$\left.\begin{array}{l} \rho_{-1}^n = \rho_2^n \ \ , \ u_{-1}^n = u_2^n \ \ , \ \ p_{-1}^n = p_2^n \\ \rho_{I+2}^n = \rho_{I-1}^n \ \ , \ u_{I+2}^n = u_{I-1}^n \ \ , \ \ p_{I+2}^n = p_{I-1}^n \end{array}\right\} . \tag{4.42}$$

Toro presents four weight limiters identified as Super A, Van Leer A, Van Albada A, and Mini A and associates flux limiters Super Bee, Van Leer, Van Albada, and Mini Bee (Toro, 1999:469) with the respective weight limiters. These flux limiters are defined as

$$\psi_{sb}(r) = \begin{cases} 0, & r \le 0, \\ 2r, & 0 \le r \le 1/2, \\ 1, & 1/2 \le r \le 1, \\ r, & 1 \le r \le 2, \\ 2, & r \ge 2, \end{cases} \tag{4.43}$$

$$\psi_{vl}(r) = \begin{cases} 0, & r \leq 0, \\ \dfrac{2r}{1+r}, & r \geq 0, \end{cases} \tag{4.44}$$

$$\psi_{va}(r) = \begin{cases} 0, & r \leq 0, \\ \dfrac{r(1+r)}{1+r^2}, & r \geq 0, \end{cases} \tag{4.45}$$

$$\psi_{mb}(r) = \begin{cases} 0, & r \leq 0, \\ r, & 0 \leq r \leq 1, \\ 1, & r \geq 1. \end{cases} \tag{4.46}$$

and are plotted in Figure 4.11.

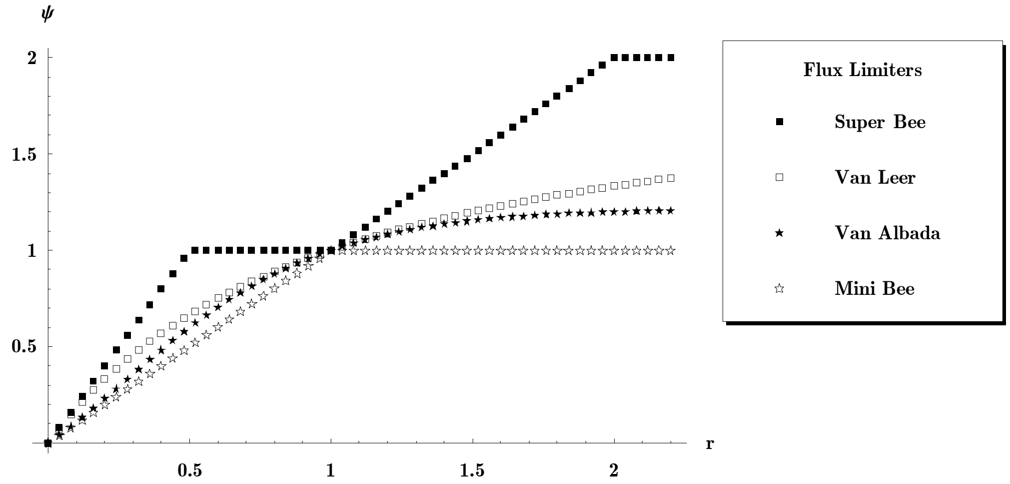

Figure 4.11. Flux Limiter Comparison

The flow parameter, coupled with flux and weight limiter functions, provides adaptive adjustments to flux weight calculations based upon local conditions resulting from Riemann problem solutions. The flow parameter effectively measures the smoothness of solutions. When the upwind and local density gradients are comparable, r approaches one, flows are characterized as smooth, and downwind flux contributions are included to guarantee second-order accuracy of solutions (Toro, 1999:457). However, as $r >> 1$, flows become discontinuous, imposing adaptive adjustment to flux calculations. Inspection of flux limiter functions (4.43) - (4.46) and Figure 4.11 shows fluxes are regulated as r becomes large. Specifically, when r exceeds one, upwind flux contributions are maximized to ensure stability, while downwind flux contributions are limited in order to restrict the downwind flux components that produce false fluctuations near discontinuous regions.

With TVD methods fully introduced, the weighted average state of each primitive variable must be determined. A TVD scheme, analogous to equation (4.29) is given as

$$\overline{\mathbf{W}}_{i+1/2} = \sum_{k=1}^{N+1} \beta_{k,LWAF}\ \mathbf{W}^{(k)}_{i+1/2} \tag{4.47}$$

where

$$\begin{aligned} \beta_{1,LWAF} &= \frac{1}{2}(1 + \phi_1 Sign(c_1)), \\ \beta_{2,LWAF} &= \frac{1}{2}(\phi_2 Sign(c_2) - \phi_1 Sign(c_1)), \\ \beta_{3,LWAF} &= \frac{1}{2}(\phi_3 Sign(c_3) - \phi_2 Sign(c_2)), \\ \beta_{4,LWAF} &= \frac{1}{2}(1 - \phi_3 Sign(c_3)). \end{aligned} \tag{4.48}$$

Finally, limited weighted average flux is determined merely by applying equation (2.6) to the LWAS variables.

Application of the flux and weight limiters to the benchmark shock tube test produced results depicted in Figure 4.12, Figure 4.13, and Figure 4.14. Figure 4.12 indicates that each flux limiter effectively eliminates spurious oscillations near the shock and contact surface discontinuities. Figure 4.13 and Figure 4.14 reveal detailed behavior of each limiter function in the two regions of interest. Figure 4.13 indicates that the Super Bee flux limiter function performs best at the contact surface, while the Van Leer function provides more graphically consistent results, compared to exact solutions, than the remaining three functions at this discontinuity. Inspection of Figure 4.14 demonstrates sporadic behavior of the Super Bee function at the shock front, while the Van Leer limiter best eliminates oscillations at the discontinuity. Therefore, the Van Leer flux limiter is presumed best for shock modeling and will be implemented for all subsequent calculations.

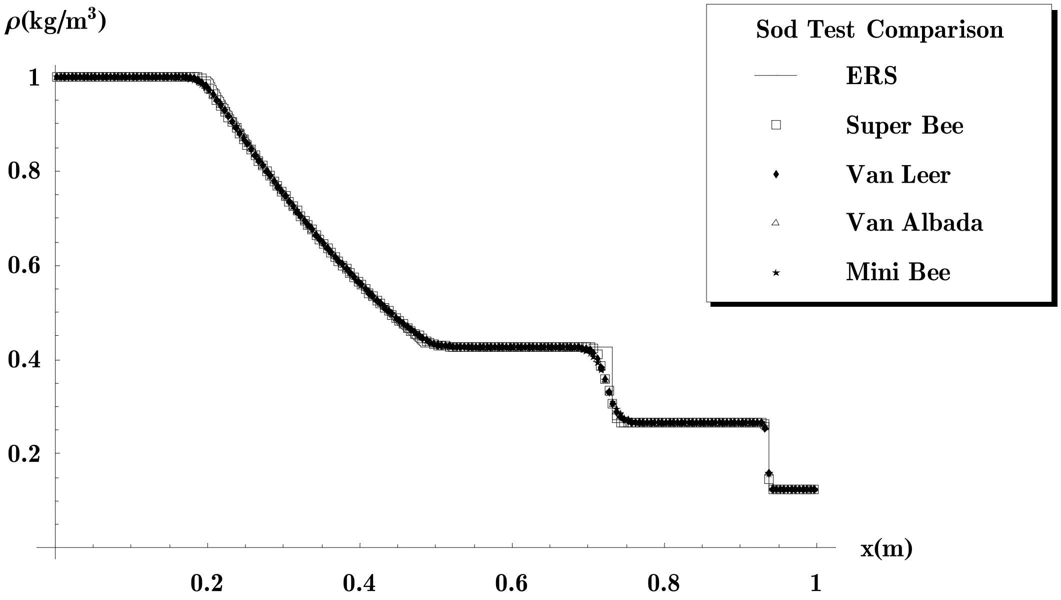

Figure 4.12. Flux Limiter Sod Test Density Comparison

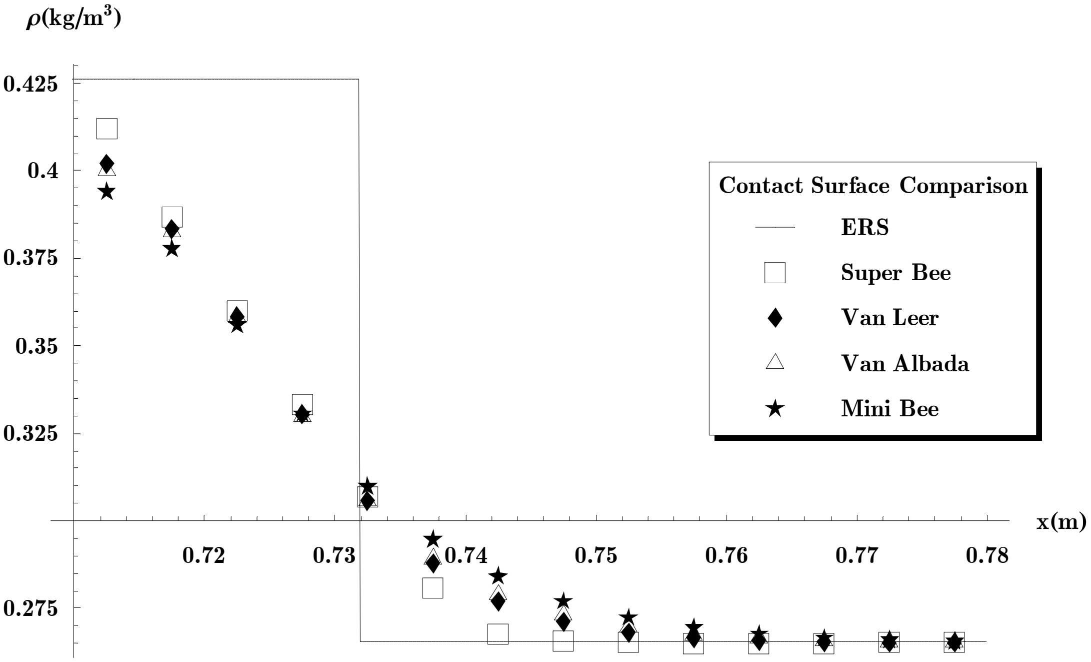

Figure 4.13. Contact Surface Flux Limiter Density Comparison

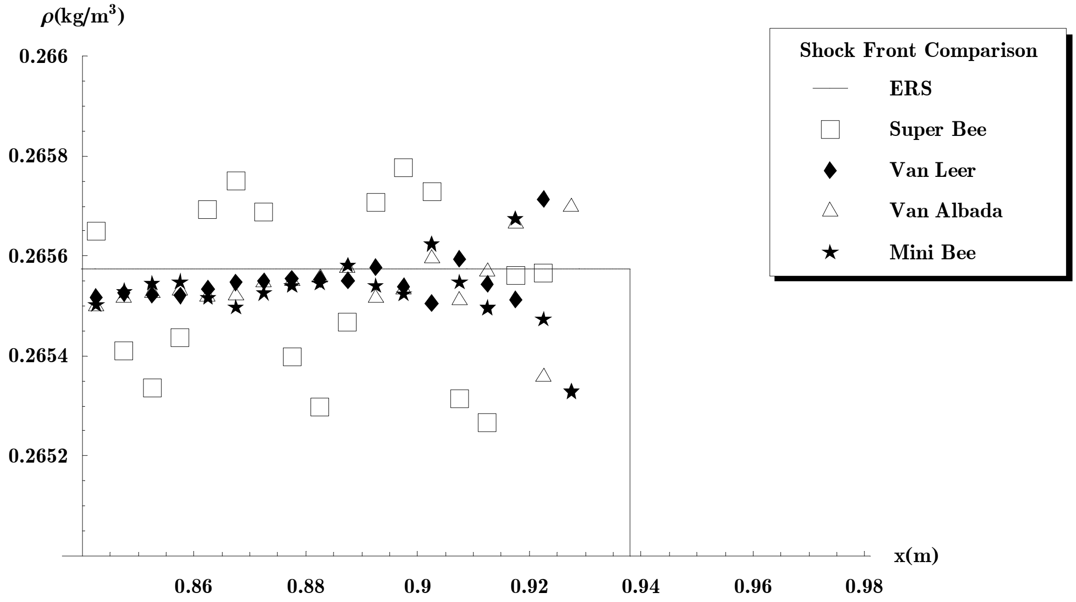

Figure 4.14. Shock Front Flux Limiter Density Comparison

4.11. Verification of Second-Order Accuracy

The primary objective of numerical techniques is to determine accurate approximations to exact solutions. The order of accuracy of an implemented scheme measures the amount by which exact solutions differ from discrete numerical solutions such that (Slater, 2000)

$$E = \left| f(h) - f_{exact} \right| = Ch^p \,. \tag{4.49}$$

E represents absolute error; $f(h)$ and f_{exact} symbolize approximate and exact solutions, respectively; C is a constant; and h is a measure of grid spacing with order of accuracy p where

$$h^p = \left(\frac{b-a}{n} \right)^p . \tag{4.50}$$

Here, a and b represent lower and upper domain limits, while n denotes the number of subintervals used to discretize $[a,\ b]$. It follows from (4.49) that

$$\frac{E}{h^p} = \frac{\left|f(h) - f_{exact}\right|}{h^p} = C\,, \tag{4.51}$$

which predicts that finite volume error calculations for p =2 using varying mesh sizes are expected to yield a constant, for a second-order accurate scheme.

Confirmation of second-order accurate solutions was examined by comparing exact solutions from the benchmark shock test against solutions calculated using the TVD LWAF Godunov scheme with several mesh sizes. Sample points were selected from each of the four Riemann problem states and analyzed for error and order accuracy. Table 4.1 depicts this comparison in the left star state.

n	E	E/h	E/h^2
25	0.00133348	0.033337	0.833425
50	0.00232385	0.116192	5.80962
200	0.000166184	0.0332369	6.64738
400	0.000031504	0.0126019	5.04076
800	4.78943×10^{-6}	0.00383155	3.06524
1600	1.33387×10^{-6}	0.00213420	3.41472
3200	5.98817×10^{-7}	0.00191621	6.13188
6400	4.07474×10^{-7}	0.00260783	16.6901
12800	2.64006×10^{-7}	0.00337928	43.2547

Table 4.1. Error Comparison for Density in Left Star State

If the scheme is, in fact, second-order accurate, the results in column four of Table 4.1 are expected to converge to a constant. Similarly, a first-order accurate scheme would produce convergent results in column three of the table. Column two of the table indicates that solutions begin to converge as the mesh size is refined from 500 to 1000 cells. However, at first glance, neither column three nor column four appears to converge to a constant along this interval, and the order of accuracy of the scheme cannot be definitively stated.

Because the magnitudes of the values in the respective columns differ by several orders, the error was further analyzed using a log-log plot. Specifically, taking the log of both sides of equation (4.49) yields

$$\log E = \log C + p \log h \tag{4.52}$$

which indicates that the logarithmic error varies linearly with mesh size, h, and slope p. Figure 4.15 shows data sets generated from (4.52), using $p = 1$, $p = 2$, and mesh sizes from Table 4.1, as compared to error calculated from the left star state of the computational model with the same parameters. The figure indicates error data generated using the developed one-dimensional code more closely resemble data produced from (4.52) with $p = 2$. The same analysis was conducted using data from the right star state, and produced similar results.

Because the generated results show better graphical correlation to second-order accuracy, as compared to first-order accuracy, the TVD LWAF Godunov scheme, empirically, exhibits second-order accuracy.

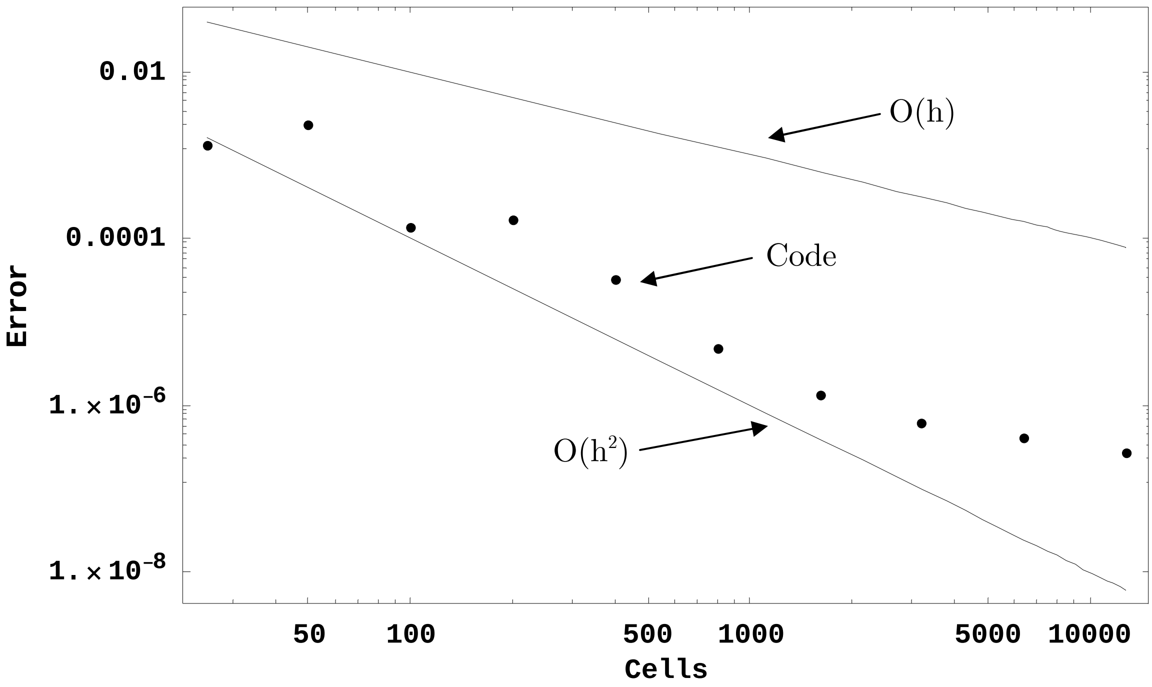

Figure 4.15. Log-Log Plot of Error vs. Number of Cells in Left Star State

4.12. Validation of the One-Dimensional Shock Code

4.12.1. Sod Test in One Dimension

During each step of code development, calculated data were compared against the Sod shock test data computed with an exact Riemann solver. Graphical evaluation of these data sets verified proper implementation of each introduced numerical technique. In addition to the Sod test, generated data from four diverse shock tests, discussed in Chapter 3, were compared graphically to results produced by the ERS. Numerical results proved consistent with published data for all tests. Finally, in order to guarantee accuracy, validation of the developed code against experimental data is required.

4.12.2. Army Research Laboratory (ARL) 57cm Shock Test

In 1996, the Army Research Laboratory (ARL) used measurements obtained in their 57cm shock tube facility to validate a second-order accurate single dimensional shock code. The shock tube was 100m long with a diameter of 57cm and contained a driver region 0.91m long (Schraml, 1996; Wittig, 1999:72). The following conditions existed at the beginning of the experiment.

$$\mathbf{W}(x,0) = \begin{cases} \mathbf{W}_{\mathrm{L}} = (4.486\,\mathrm{kg/m^3},\ 0.0\,\mathrm{m/sec},\ 379.2\times 10^3\,\mathrm{N/m^2}) & x < 0, \\ \mathbf{W}_{\mathrm{R}} = (1.208\,\mathrm{kg/m^3},\ 0.0\,\mathrm{m/sec},\ 102.1\times 10^3\,\mathrm{N/m^2}) & x > 0. \end{cases} \tag{4.53}$$

An overpressure history was collected from a measurement station located 31.48m from the initial discontinuity. Figure 4.16 portrays overpressure history data determined experimentally and computationally by ARL. The shock front arrived at the experimental measurement station at 66.0ms with a measured overpressure of 66.3kPa (Schraml, 1996; Wittig, 1999:73).

Using the developed LWAF one-dimensional code to accurately model the ARL experiment and, ultimately, validate the overpressure at the shock front requires, first, time of arrival calibration. To verify correct time of arrival of the shock front, a symmetry boundary was placed at $x = 0$m while a transmissive boundary was positioned at $x = 50$m. This far right boundary location reduced execution time without affecting results at the computational measurement station at $x = 31.48$m (Wittig, 1999:74). The computational domain was

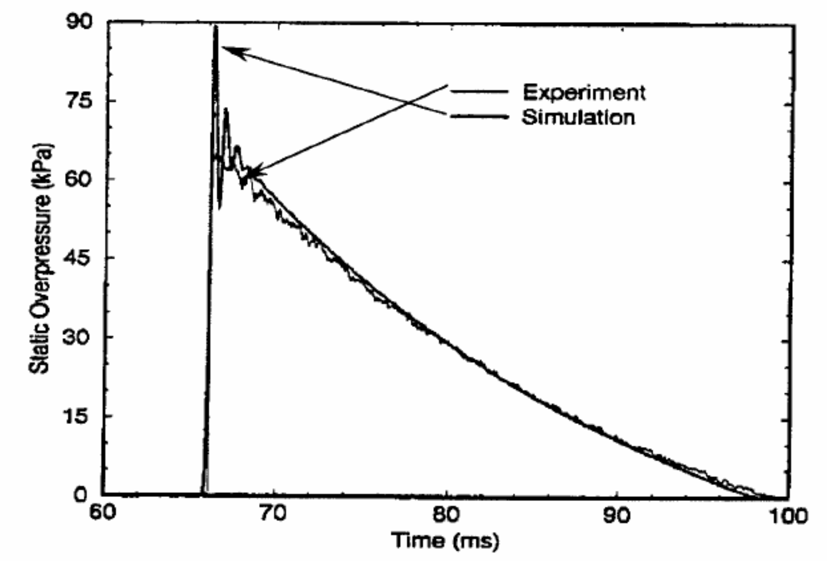

Figure 4.16. ARL Overpressure History at 31.48m

discretized into 5000 cells during the time interval [0, 100] msec, a CFL coefficient of 0.9 was applied, and the van Leer flux limiter function used.

Code execution using these initial conditions generated a later time of arrival, by 0.61ms (0.9% relative error), and a lower static overpressure, by 6.6kPa (10.0% relative error), than observed during the ARL experiment. To resolve these discrepancies, the code was re-executed using varying mesh sizes and CFL coefficients. Table 4.2 summarizes the results of mesh refinement, using a CFL coefficient of 0.9, for all computations.

Because mesh refinement did not significantly alter shock time of arrival, calculations were repeated using several CFL coefficients and a mesh size of 5000 cells, to maximize computational efficiency. Table 4.3 summarizes the results of these calculations.

n	*Time steps (CFL = 0.9)*	*Time of Arrival (msec)*	*Max Static Overpressure (kPa)*
5000	5623	66.61	59.7
6000	6750	66.62	59.3
7000	7875	66.63	59.9
8000	8999	66.69	59.7
9000	10123	66.70	59.4
10000	11250	66.71	59.9

Table 4.2. Mesh Refinement Effects on Time of Arrival and Static Overpressure

CFL	*Time steps (CFL = 0.9)*	*Time of Arrival (msec)*	*Max Static Overpressure (kPa)*
0.9	5623	66.61	59.7
0.8	6310	66.54	58.8
0.6	8410	66.48	58.8
0.4	12609	66.44	58.7
0.2	25208	66.45	58.6
0.1	50412	66.49	58.6

Table 4.3. CFL Refinement Effects on Time of Arrival and Static Overpressure

As with mesh refinement, CFL coefficient modification did not produce significant changes to time of arrival or static overpressure. Because the objectives of these refinements were to decrease time of arrival and increase overpressure, data from the above tables were examined to predict the most favorable combination of mesh size and CFL coefficient. Based on this analysis, a final computation was run using a mesh of 7000 cells with a CFL coefficient of 0.4. Again, solutions failed to improve. Finally, in order to minimize the possibility of false reflections at the computationally transmissive boundary, several simulations were completed by modifying the location of the far right boundary from 60m to 100m. Solutions did not improve, and I concluded that the discrepancies resulted from the simplifying assumptions, inherent in the Euler conservation equations, which neglect the physical effects of viscosity and heat transfer.

In the end, achieving the correct arrival time required increasing the initial conditions in the driver region by five percent to

$$\mathbf{W}(x,0) = \begin{cases} \mathbf{W}_{\mathrm{L}} = (4.710\,\mathrm{kg/m^3},\ 0.0\,\mathrm{m/sec},\ 398.1\times 10^3\,\mathrm{N/m^2}) & x < 0, \\ \mathbf{W}_{\mathrm{R}} = (1.208\,\mathrm{kg/m^3},\ 0.0\,\mathrm{m/sec},\ 102.1\times 10^3\,\mathrm{N/m^2}) & x > 0. \end{cases} \tag{4.54}$$

Figure 4.17 illustrates overpressure history data at the computational measurement station. As depicted in Figure 4.18, compared to ARL computational results, the LWAF generated data proves smooth at the shock front (a result of application of the TVD flux and weight limiter functions).

The developed LWAF single dimensional code predicted shock arrival at the computational measurement station after 66.03ms, and a peak overpressure at the shock front of 62.4kPa. Because the predicted overpressure agreed with the experimental overpressure within 5.9%, I concluded the developed computational model correctly models shocks. Confident that the implemented single-dimensional techniques are sound, the numerical procedures are next extended into two and three dimensions.

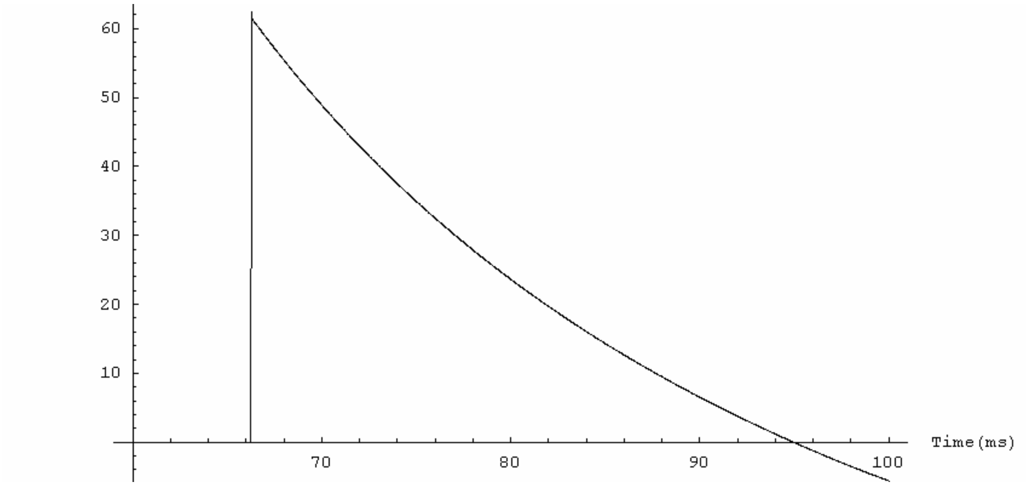

Figure 4.17. LWAF Overpressure History at 31.48m

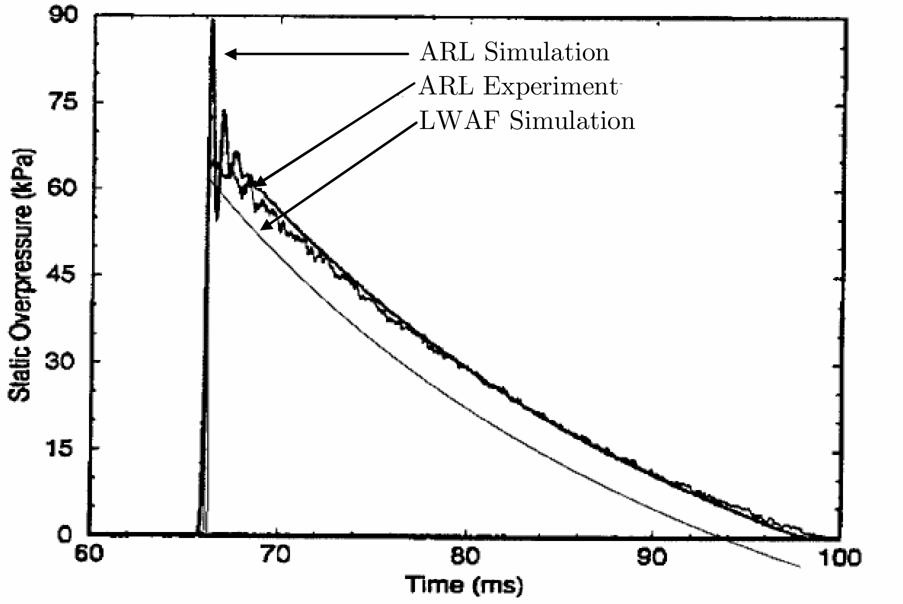

Figure 4.18. Overpressure History Comparison at 31.48m

5. *Code Implementation in Multiple Dimensions*

5.1. *Overview*

The fully developed, single-dimensional, second-order accurate LWAF solver is applied to two and three-dimensional schemes for non-linear hyperbolic systems of equations. Finite volume techniques are introduced and applied to the time-dependent Euler conservation equations in multiple dimensions. Special considerations and improvements to computational efficiency are addressed. Finally, the developed multi-dimensional computational models are validated against the one-dimensional benchmark shock tube test, as well as mild cylindrical and spherical shock tests, and compared to published results.

5.2. *Implementation in Two Dimensions*

5.2.1. *Initial Boundary Value Problem*

The two-dimensional initial boundary value problem for non-linear systems of hyperbolic conservation laws, assuming uniform flow in the z-direction is

$$\begin{aligned} &\mathit{PDEs}: \ \mathbf{U}_t + \mathbf{F}(\mathbf{U})_x + \mathbf{G}(\mathbf{U})_y = \mathbf{0}, \\ &\mathit{ICs}: \quad \mathbf{U}(x, y, 0) = \mathbf{U}^{(0)}(x,y). \end{aligned} \tag{5.1}$$

Here $\mathbf{U}^{(0)}(x,y)$ is a piecewise continuous distribution of initial data defined over the spatial domain $[0, \mathrm{L_x}]$ x $[0, \mathrm{L_y}]$ at $t = 0$. Finally, in two dimensions, boundary conditions are described along a line at each of the four boundaries using symmetric and transmissive boundaries, as described in the one-dimensional case.

5.2.2. Discretization of the Euler Conservation Equations

Discretization of the spatial and temporal computational domain [0, L_x] x [0, L_y] x [0, T] requires extension of the single-dimensional mesh in the *y*-direction. The spatial mesh is partitioned into $I \times J$ computational cells of uniform area $\Delta x \times \Delta y$ such that

$$\begin{aligned} \Delta x &= \frac{L_x}{I}, \\ \Delta y &= \frac{L_y}{J}. \end{aligned} , \tag{5.2}$$

Each computational cell is bounded by faces $i - 1/2$ and $i + 1/2$ in the *x*-direction, and faces $j - 1/2$ and $j + 1/2$ in the *y*-direction where

$$\begin{aligned} x_{i-1/2} &= (i-1)\Delta x, \\ x_{i+1/2} &= i\Delta x, \\ y_{j-1/2} &= (j-1)\Delta y, \\ y_{j+1/2} &= j\Delta y. \end{aligned} \tag{5.3}$$

The center of each computational cell (i, j) is determined as

$$(x_i, y_j) = ((i - \frac{1}{2})\Delta x, (j - \frac{1}{2})\Delta y). \tag{5.4}$$

As in the single-dimensional case, the temporal domain is separated into n non-uniform time steps which are determined, adaptively, as

$$\Delta t = \min\left(\frac{C_{cfl}\Delta x}{(S_i^n)_{\max}}, \frac{C_{cfl}\Delta y}{(S_j^n)_{\max}}\right). \tag{5.5}$$

Similarly, $(S_i^n)_{max}$ and $(S_j^n)_{max}$ are approximations for maximum wave speeds in the x and y directions, respectively, during time level n, and are based upon the material and sound speeds where

$$\begin{aligned} (S_i^n)_{\max} &= \max\left\{\left|u_{i,j}^n\right| + a_{i,j}^n\right\}, \\ (S_y^n)_{\max} &= \max\left\{\left|v_{i,j}^n\right| + a_{i,j}^n\right\} \end{aligned} \tag{5.6}$$

The conditions established in (5.5) and (5.6), coupled with the CFL coefficient restriction defined in Chapter 4, predict waves in the solution of Riemann problems that remain spatially confined within cell limits defined in (5.3) for every time step. This prediction correlates directly to solution stability in multiple dimensions.

5.2.3. Dimension Splitting

The dimension splitting technique permits resolving the two dimensional IBVP (5.1) as two single-dimensional IBVPs. A simple version of this approach replaces (5.1) by the sequence of IVPs (Toro, 1999:541)

$$\left.\begin{aligned} &PDEs: \ \mathbf{U}_t + \mathbf{F}(\mathbf{U})_x = 0, \\ &ICs: \quad \mathbf{U}_{i,j}^n \end{aligned}\right\} \overset{\Delta t}{\Rightarrow} \mathbf{U}_{i,j}^{n+1/2} \tag{5.7}$$

and

$$\left.\begin{array}{ll} PDEs: & \mathbf{U}_t + \mathbf{G}(\mathbf{U})_y = 0, \\ ICs: & \mathbf{U}_{i,j}^{n+1/2} \end{array}\right\} \overset{\Delta t}{\Rightarrow} \mathbf{U}_{i,j}^{n+1}. \tag{5.8}$$

The solution $\mathbf{U}_{i,j}^{n+1/2}$ is obtained via (5.7) by solving J one-dimensional problems in the x-direction. This solution provides initial conditions to subsequently solve (5.8) using I one-dimensional problems in the y-direction in order to, ultimately, determine $\mathbf{U}_{i,j}^{n+1}$. In operator notation (5.7) - (5.8) may be written

$$\mathbf{U}_{i,j}^{n+1} = Y^{(\Delta t)} X^{(\Delta t)} (\mathbf{U}_{i,j}^{n}) \tag{5.9}$$

where $X^{(\Delta t)}$ and $Y^{(\Delta t)}$ represent approximate time step solution operators to the IBVP. There is no specific purpose for applying the operators in the order described. Accordingly, an equivalent scheme is

$$\mathbf{U}_{i,j}^{n+1} = X^{(\Delta t)} Y^{(\Delta t)} (\mathbf{U}_{i,j}^{n}) \tag{5.10}$$

It can be shown that (5.9) and (5.10) are first-order accurate during each time step, given that the individual operators $X^{(\Delta t)}$ and $Y^{(\Delta t)}$ are at least first-order accurate (Toro, 1999:542). Because the desired solution must be, spatially, second-order accurate, Toro presents two schemes that satisfy the accuracy requirement every other time step as

$$\mathbf{U}_{i,j}^{n+2} = X^{(\Delta t)} Y^{(\Delta t)} Y^{(\Delta t)} X^{(\Delta t)} (\mathbf{U}_{i,j}^{n}) \tag{5.11}$$

and

$$\mathbf{U}_{i,j}^{n+2} = Y^{(\Delta t)} X^{(\Delta t)} X^{(\Delta t)} Y^{(\Delta t)} (\mathbf{U}_{i,j}^{n}). \tag{5.12}$$

In practice, (5.11) is implemented over the interval $[t^n, t^{n+2}]$ based upon the following method. Given initial conditions $\mathbf{U}_{i,j}^n$, boundary conditions are established as symmetric or transmissive and a stable time step is approximated via (5.5). The first of two time steps begins with $X^{(\Delta t)}$ operating on $\mathbf{U}_{i,j}^n$. Specifically, in the x-direction, J one-dimensional Riemann problems are solved, fluxes are calculated at each computational boundary, and temporary variable solutions are updated in each cell as $\widetilde{\mathbf{U}}_{i,j}^{n+1}$. Next, boundary conditions are updated along the lines $y = 0$ and $y = L_y$ and $Y^{(\Delta t)}$ operates on $\widetilde{\mathbf{U}}_{i,j}^{n+1}$ by solving I one-dimensional problems in the y-direction, as described above. At the conclusion of this first time step, solutions are analyzed against the CFL stability criteria. If unstable solutions exist, interim solutions are discarded, the CFL coefficient and time step are re-calculated, and the time step is reset. However, provided stable solutions exist, the second time step begins.

Procedures in the second time step are executed identically to those in the first step, with one exception. Now $Y^{(\Delta t)}$ operates on $\mathbf{U}_{i,j}^{n+1}$, yielding the temporary solution $\widetilde{\mathbf{U}}_{i,j}^{n+2}$, upon which $X^{(\Delta t)}$ subsequently operates. This reversal of operations effectively eliminates the y-directional biased solution $\mathbf{U}_{i,j}^{n+1}$ present at the end of the first time step and produces the desired second-order accurate solution $\mathbf{U}_{i,j}^{n+2}$ at the conclusion of the second time step. Subject to solution stability verification, simulation time is advanced by $2\Delta t$. Finally, this second-order accurate scheme is executed, forward in time, until the desired solution time is reached.

5.2.4. Special Considerations

The dimension splitting technique facilitates solving the Euler conservation equations, in the x-direction, as

$$\begin{bmatrix}\rho \\ \rho u \\ E \\ \rho v\end{bmatrix}_t + \begin{bmatrix}\rho u \\ \rho u^2 + p \\ E(u+p) \\ \rho v u\end{bmatrix}_x = \mathbf{0}\,, \tag{5.13}$$

and in the y-direction

$$\begin{bmatrix}\rho \\ \rho v \\ E \\ \rho u\end{bmatrix}_t + \begin{bmatrix}\rho v \\ \rho v^2 + p \\ E(v+p) \\ \rho u v\end{bmatrix}_y = \mathbf{0}\,. \tag{5.14}$$

Note the first, second, and third equations in system (5.13) appear identical to the pure one-dimensional problem in the x-direction. In this system, u represents the normal component of material velocity, while v represents the tangential, or shear, component. Similarly, in system (5.14), v denotes the normal velocity component, while u symbolizes the tangential component. Consideration of tangential velocities introduces corresponding tangential momentum terms and fluxes which appear in the fourth equations of both systems. Furthermore, inspection of the systems demonstrates these shear velocities contribute to total energy density determination as

$$E = \frac{1}{2}\rho(u^2 + v^2 + w^2) + \frac{p}{\gamma - 1}\,. \tag{5.15}$$

Solutions to (5.13) and (5.14) that apply TVD flux limiter functions produce the dissipative wave structure of Figure 5.1.

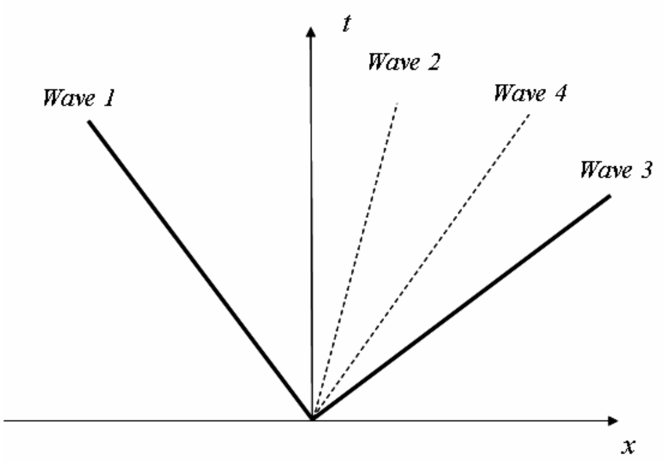

Figure 5.1. Two-Dimensional TVD Flux Limiter Wave Structure

This arrangement dictates normal and tangential flux calculations, which are completed separately. Recall from Chapter 4 that, in a single dimension, conserved variables fluxes are calculated by determining the weighted average state of primitive variables. In the two-dimensional case, the weighted average states of density, normal velocity, and pressure are determined using equations (4.43) and (4.44). These primitive variable weighted average states permit computation of fluxes for mass, normal momentum, and energy.

Calculation of the tangential velocity WAS and the corresponding tangential momentum flux and energy flux requires special treatment. To determine the former requires application of the equations (Toro, 1999:550)

$$\overline{V}_{T,i+1/2} = \beta_{5,LWAF} V_{T,1} + \beta_{6,LWAF} V_{T,4} \tag{5.16}$$

where V_T represents the tangential velocity and the TVD weights are

$$\beta_{5,LWAF} = (1 + \phi_4 Sign(c_4)) \tag{5.17}$$

and

$$\beta_{6,LWAF} = (1 - \phi_4 Sign(c_4)). \tag{5.18}$$

The eigenvalue structure of solutions to (5.13) and (5.14) conveniently dictates $c_4 = c_2$ (Toro, 1999:548). However, determination of ϕ_4 is not as trivial. Unlike weight limiter functions ϕ_1, ϕ_2, and ϕ_3, which depend on the density gradient across the local and upwind waves, $\phi_4(r_4)$ is calculated from tangential velocity gradients ΔV_T as

$$r_{i+1/2,4} = \frac{\Delta V_{T[i+1/2-(Sign(c_4)),4]}}{\Delta V_{T[i+1/2,4]}}. \tag{5.19}$$

Calculation of all components required to solve systems (5.13) and (5.14) is complete.

5.2.5. Sod Test in Two Dimensions

Because the benchmark shock tube test consists of flows in a single direction, correct modeling of planar flows in two dimensions is readily verified. Accordingly, the two dimensional Sod test was executed over the square domain [0, 1m] x [0, 1m] consisting of 100 cells in the x and y directions and a diaphragm, positioned along the line $x = 0$m. Initial conditions were established as

$$\mathbf{W}(x,y,0) = \begin{cases} \mathbf{W}_L = (1.000\ \mathrm{kg/m^3}, 0.0\,\mathrm{m/sec}, 0.0\,\mathrm{m/sec}, 1.0\,\mathrm{N/m^2}) & x < 0.5\mathrm{m}, \\ \mathbf{W}_R = (0.125\,\mathrm{kg/m^3}, 0.0\,\mathrm{m/sec}, 0.0\,\mathrm{m/sec}, 0.1\,\mathrm{N/m^2}) & x > 0.5\mathrm{m}. \end{cases} \tag{5.20}$$

and solutions developed over the time interval $t = [0,\ 0.25\ \text{sec}]$. The density profile at $t = 0.25$ sec is depicted below.

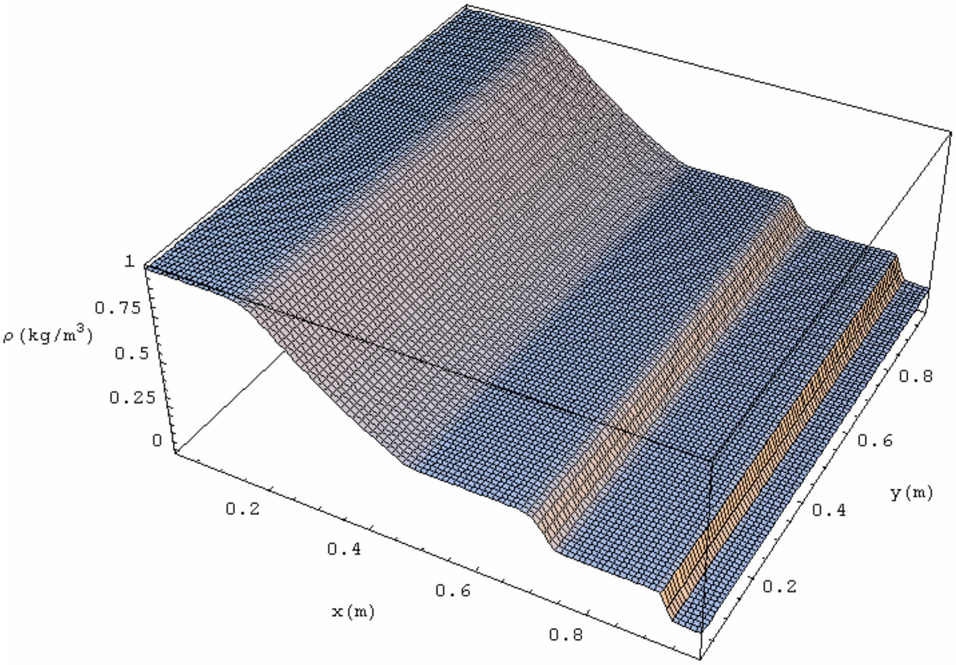

Figure 5.2. Two-Dimensional Sod Density Profile at $t = 0.25$ sec

To ensure planar flows modeled in two dimensions are consistent with the one-dimensional Sod test density data from the two-dimensional test was extracted from the first set of cells in the y-direction. These results are compared to the exact solution, as well as the second-order accurate solution obtained by the LWAF method in a single dimension, in Figure 5.3. The second-order accurate solutions appear graphically identical for both dimensions.

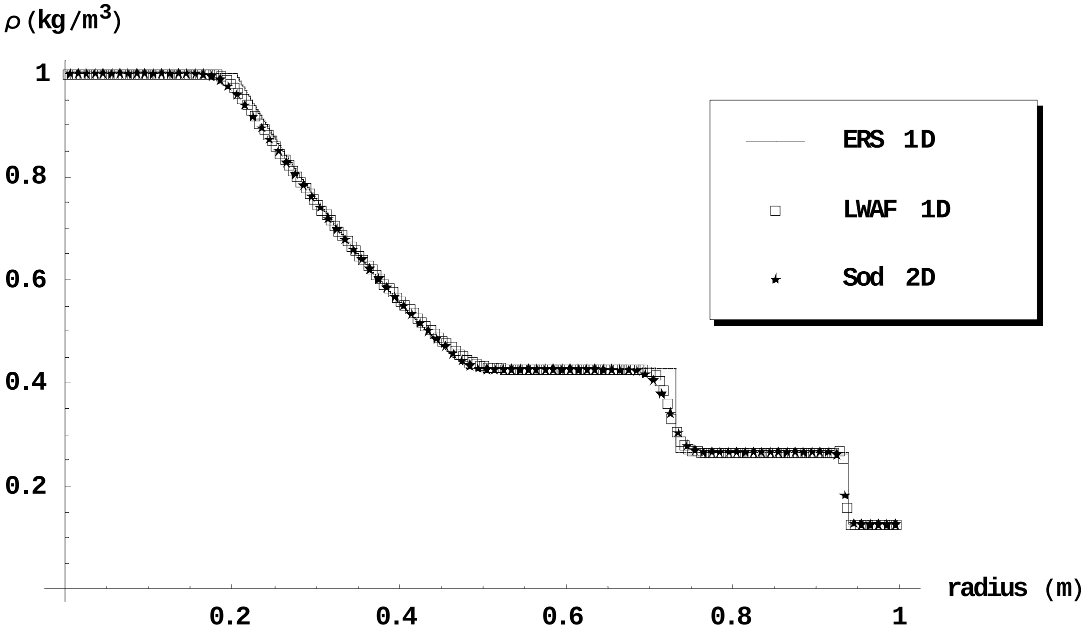

Figure 5.3. One and Two-Dimensional Sod Density Profiles at $t = 0.25$ sec

5.2.6. Mild Cylindrical Shock Test

To verify that the developed code correctly models flows in two dimensions, the Euler equations were solved over the square domain [0, 2m] x [0, 2m] discretized as a computational mesh of 100 cells in the x and y directions. The initial conditions consisted of a circular region with radius 0.4m, centered at

(1,1), with primitive variables of $\mathbf{W}_L$ and $\mathbf{W}_R$ from (5.20) representing states inside and outside the circle, respectively (Toro, 1999:583). Figure 5.4 shows the density profile at $t = 0.25$ sec. Inspection of the profile indicates, as expected, a solution which exhibits a circular shock, contact surface, and rarefaction.

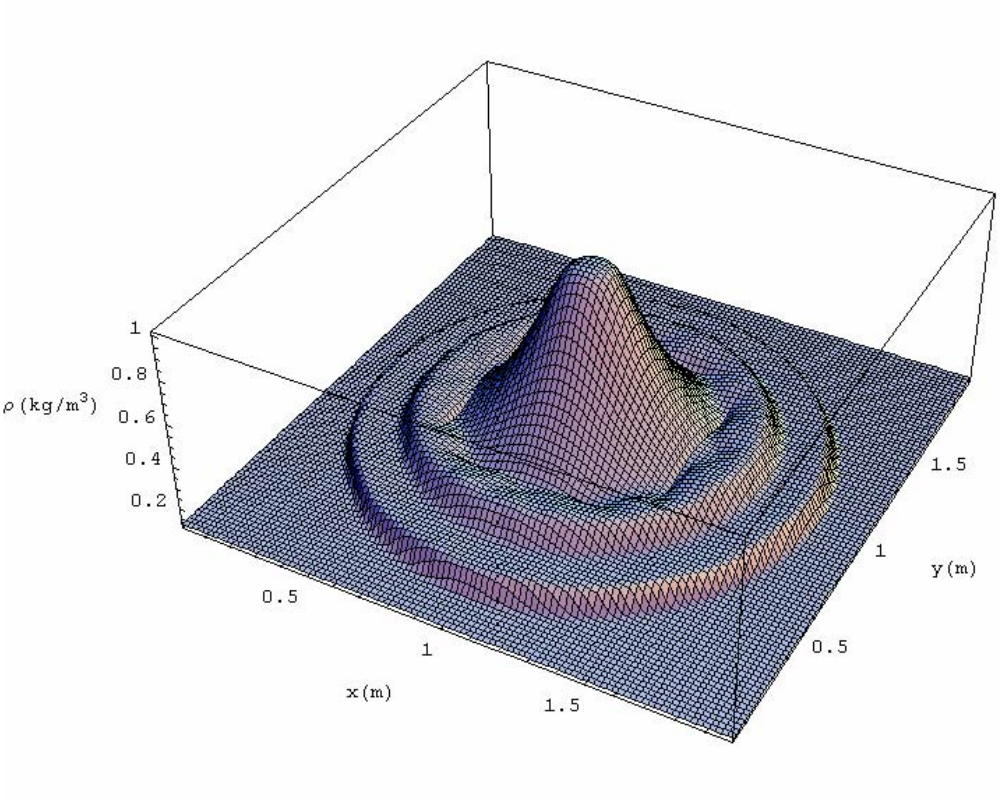

Figure 5.4. Cylindrical Explosion Density Profile at t = 0.25 sec

The density profile indicates the presence of potential numerical artifacts in the region between the rarefaction and contact discontinuity. Accordingly, graphical resolution, in addition to circular symmetry, of solutions may be further examined through the contour plot in Figure 5.5. Again, the artifacts appear in the region of concern, where the solutions appear to lack resolution. Doubling the cells in both directions from 100 to 200 reduced the oscillations in the region of concern, as shown in Figure 5.6. As expected, the graphical output shows fewer oscillations and better circular symmetry with mesh refinement.

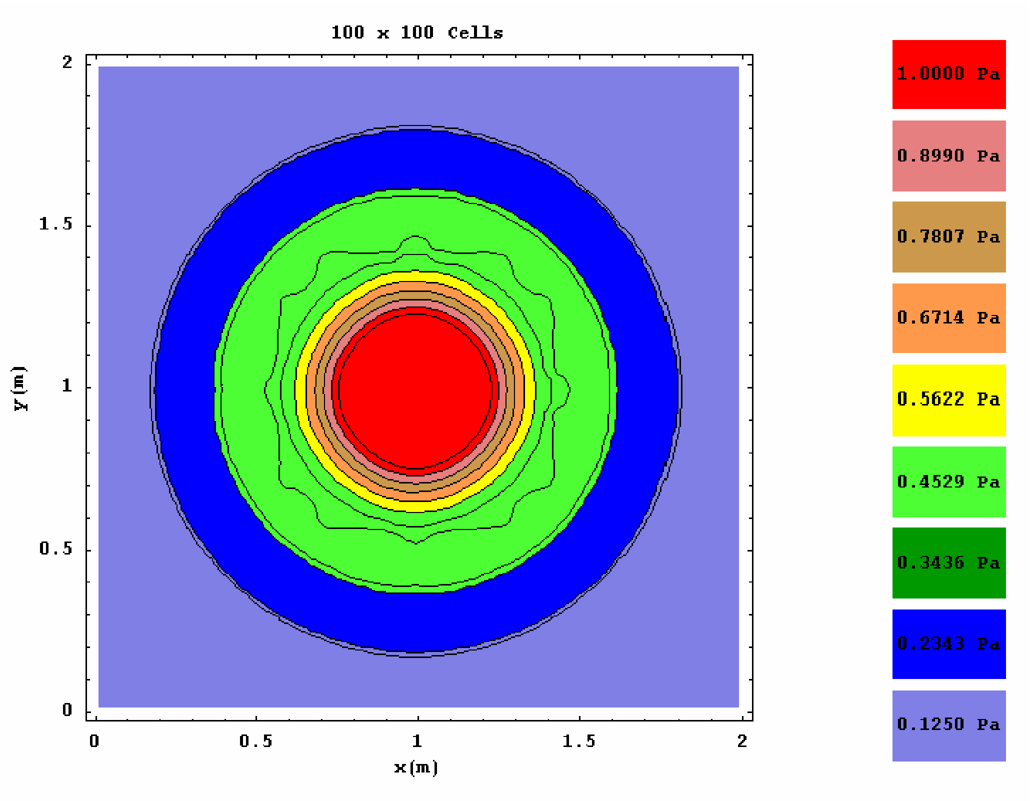

Figure 5.5. Cylindrical Explosion Density Contours at $t = 0.25$ sec

The same test was conducted using a mesh of 400 cells in each direction. Doubling the cells again did not appear to significantly change solutions, either graphically or numerically. Additionally, increasing the number of time steps by modifying the stability condition did not reduce the contour fluctuations and it's likely the oscillations are an artifact associated with the numerical viscosity inherent in the LWAF scheme. Recall TVD weight limiting is analogous to artificial viscosity methods. Because the two-dimensional code applies weight limiting at every cell interface at every time step, it's conceivable the artificial viscosity manifests itself, as time progresses, as numerical error.

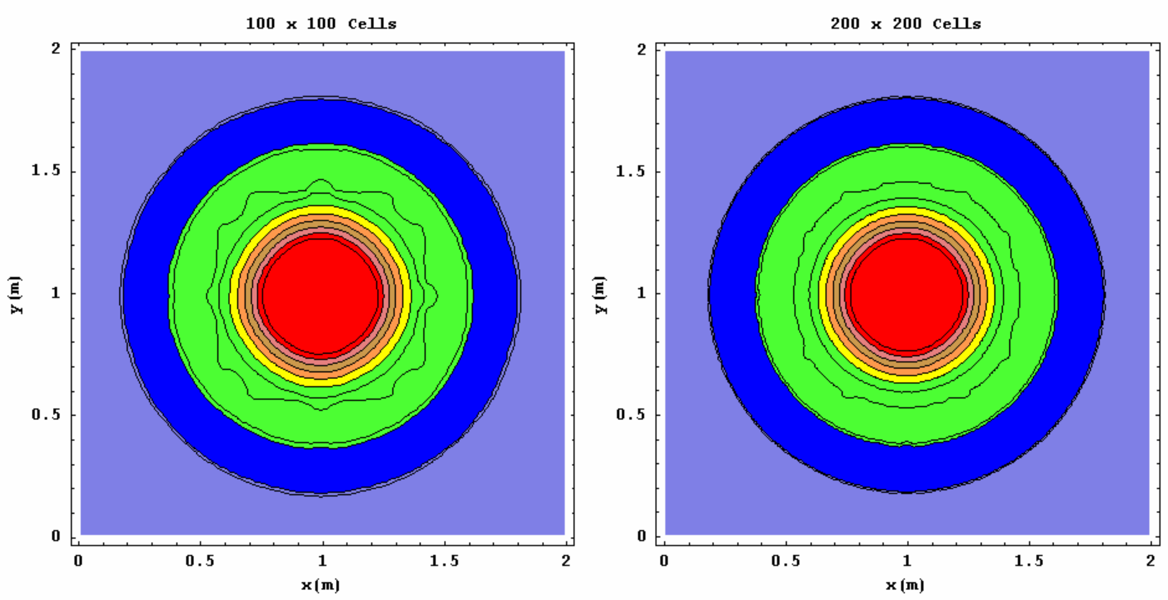

Figure 5.6. Cylindrical Explosion Density Profile Mesh Refinement

As an additional verification of circular symmetry, densities were compared along a line extending, radially, one meter outward from (1,1) at angles of $\theta = 0$, $\pi/4$, $\pi/2$, $3\pi/4$, and π, as measured from the x-axis. Figure 5.7 shows the density profiles along each of these lines and indicates nearly identical values for each angle.

Based on these analyses, I conclude two-dimensional flows are properly modeled using dimension splitting techniques.

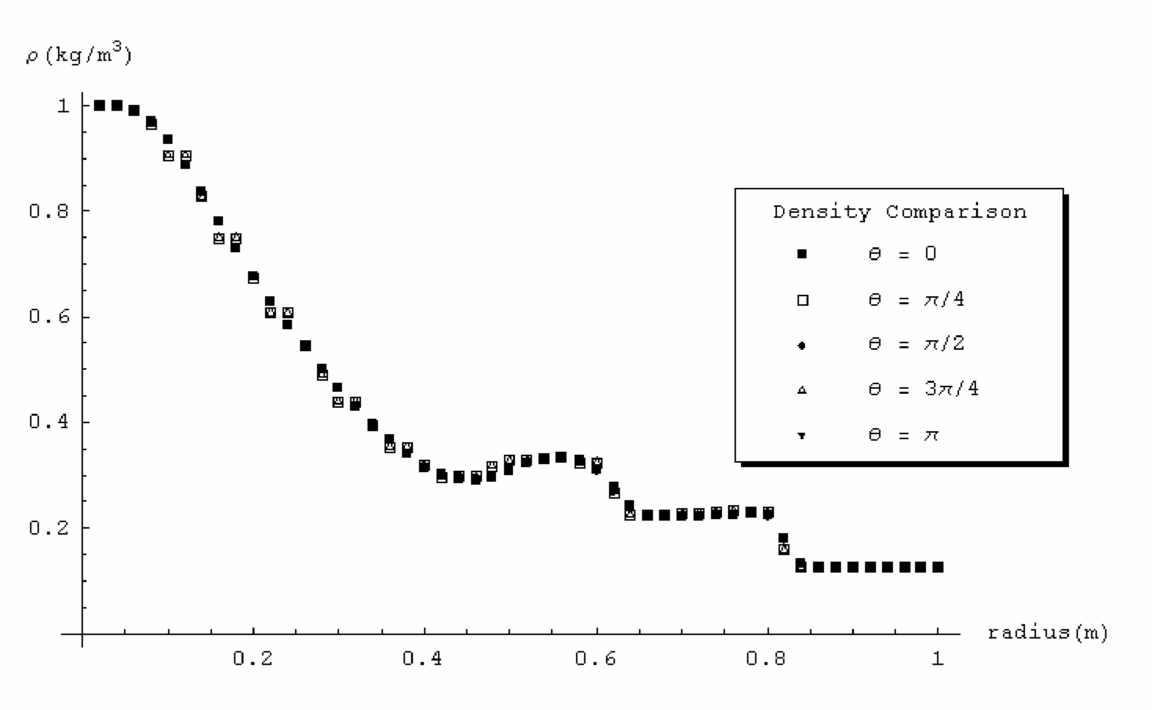

Figure 5.7. Mild Cylindrical Explosion Density Comparison at $t = 0.25$ sec

5.3. Implementation in Three Dimensions

5.3.1. Initial Boundary Value Problem

The three dimensional initial boundary value problem for non-linear systems of hyperbolic conservation laws is

$$\begin{aligned} &PDEs: \ \mathbf{U}_t + \mathbf{F}(\mathbf{U})_x + \mathbf{G}(\mathbf{U})_y + \mathbf{H}(\mathbf{U})_z = \mathbf{0}, \\ &ICs: \quad \mathbf{U}(x,y,z,0) = \mathbf{U}^{(0)}(x,y,z). \end{aligned} \tag{5.21}$$

Here $\mathbf{U}^{(0)}(x,y,z)$ is a piecewise continuous distribution of initial data defined over the spatial domain [0, L_x] x [0, L_y] x [0, L_z] at $t = 0$. Lastly, in three dimensions, boundary conditions are described along a plane at each of the six boundaries using symmetric and transmissive boundary conditions, as described in the one-dimensional case.

5.3.2. Discretization of the Euler Conservation Equations

Discretization of the spatial and temporal computational domain [0, L_x] x [0, L_y] x [0, L_z] x [0, T] requires extension of the two-dimensional mesh in the *z*-direction. The spatial mesh is partitioned into I x J x K computational cells of uniform volume $\Delta x \times \Delta y \times \Delta z$ such that

$$\begin{aligned}\Delta x &= \frac{L_x}{I},\\ \Delta y &= \frac{L_y}{J},\\ \Delta z &= \frac{L_z}{K}.\end{aligned} \tag{5.22}$$

Each computational cell is bounded by six faces $i - 1/2$, $i + 1/2$, $j - 1/2$, $j + 1/2$, $k - 1/2$, $k + 1/2$ in the x, y, and z directions, respectively, where

$$\begin{aligned}x_{i-1/2} &= (i-1)\Delta x,\\ x_{i+1/2} &= i\Delta x,\\ y_{j-1/2} &= (j-1)\Delta y,\\ y_{j+1/2} &= j\Delta y,\\ z_{k-1/2} &= (k-1)\Delta z,\\ z_{k+1/2} &= k\Delta z.\end{aligned} \tag{5.23}$$

The center of each computational cell (i, j, k) is determined as

$$(x_i, y_j, z_k) = ((i-\frac{1}{2})\Delta x,\ (j-\frac{1}{2})\Delta y,\ (k-\frac{1}{2})\Delta z). \tag{5.24}$$

As in the one and two-dimensional cases, the temporal domain is separated into n non-uniform, adaptively determined time steps where

$$\Delta t = \min\left(\frac{C_{cfl}\Delta x}{(S_i^n)_{\max}}, \frac{C_{cfl}\Delta y}{(S_j^n)_{\max}}, \frac{C_{cfl}\Delta z}{(S_k^n)_{\max}} \right). \tag{5.25}$$

$(S_i^n)_{\max}$, $(S_j^n)_{\max}$, and $(S_k^n)_{\max}$ are approximations for maximum wave speeds in the x, y, and z directions, respectively, during time level n, and are based upon the material and sound speeds such that

$$\begin{aligned} (S_i^n)_{\max} &= \max\left\{ \left| u_{i,j,k}^n \right| + a_{i,j,k}^n \right\}, \\ (S_y^n)_{\max} &= \max\left\{ \left| v_{i,j,k}^n \right| + a_{i,j,k}^n \right\}, \\ (S_z^n)_{\max} &= \max\left\{ \left| w_{i,j,k}^n \right| + a_{i,j,k}^n \right\} \end{aligned} \tag{5.26}$$

Finally, as in the one and two-dimensional models, the conditions set forth ultimately predict stable solutions across the entire computational domain during each time step.

5.3.3. Dimension Splitting

The splitting techniques executed in three dimensions are analogous to the two-dimensional procedures. Equation (5.21) is resolved as three IBVPs (Toro, 1999:543)

$$\left. \begin{array}{ll} PDEs: & \mathbf{U}_t + \mathbf{F}(\mathbf{U})_x = \mathbf{0}, \\ ICs: & \mathbf{U}_{i,j,k}^n \end{array} \right\} \overset{\Delta t}{\Rightarrow} \mathbf{U}_{i,j,k}^{n+1/3}, \tag{5.27}$$

$$\left.\begin{array}{ll} PDEs: & \mathbf{U}_t + \mathbf{G}(\mathbf{U})_y = \mathbf{0}, \\ ICs: & \mathbf{U}_{i,j,k}^{n+1/3} \end{array}\right\} \overset{\Delta t}{\Rightarrow} \mathbf{U}_{i,j,k}^{n+2/3}, \tag{5.28}$$

and

$$\left.\begin{array}{ll} PDEs: & \mathbf{U}_t + \mathbf{H}(\mathbf{U})_z = \mathbf{0}, \\ ICs: & \mathbf{U}_{i,j,k}^{n+2/3} \end{array}\right\} \overset{\Delta t}{\Rightarrow} \mathbf{U}_{i,j,k}^{n+1} \tag{5.29}$$

which may be summarized, in operator notation, as

$$\mathbf{U}_{i,j,k}^{n+1} = Z^{(\Delta t)} Y^{(\Delta t)} X^{(\Delta t)} (\mathbf{U}_{i,j,k}^{n}). \tag{5.30}$$

As in the two-dimensional case, analysis of this method indicates first-order accuracy in time. However, second-order spatial accuracy is achieved, every other time step, by the method

$$\mathbf{U}_{i,j,k}^{n+2} = X^{(\Delta t)} Y^{(\Delta t)} Z^{(\Delta t)} Z^{(\Delta t)} Y^{(\Delta t)} X^{(\Delta t)} (\mathbf{U}_{i,j,k}^{n}). \tag{5.31}$$

In practice, (5.31) is implemented over the interval $[t^n, t^{n+2}]$ based upon the following method. Given initial conditions $\mathbf{U}_{i,j,k}^{n}$, boundary conditions are established as symmetric or transmissive and a stable time step is approximated via (5.25). The first of two time steps begins with $X^{(\Delta t)}$ operating on $\mathbf{U}_{i,j,k}^{n}$. Specifically, in the x-direction, J x K one-dimensional Riemann problems are solved, fluxes are calculated at each computational boundary, and temporary variable solutions are updated in each cell as $\widetilde{\mathbf{U}}_{i,j,k}^{n+1}$. Next, boundary conditions are updated along the planes $y = 0$ and $y = L_y$ and $Y^{(\Delta t)}$ operates on $\widetilde{\mathbf{U}}_{i,j,k}^{n+1}$ by solving $I\,\mathrm{x}K$ one-dimensional problems in the y-direction, as described above, producing updated cell solutions $\widetilde{\widetilde{\mathbf{U}}}_{i,j,k}^{n+1}$. Before solving problems in the z-direction, boundary conditions are applied along the planes $z = 0$ and $z = L_z$. At last, $Z^{(\Delta t)}$ operates on $\widetilde{\widetilde{\mathbf{U}}}_{i,j,k}^{n+1}$ by solving $I\,\mathrm{x}J$ one-dimensional problems in the z-direction. At the conclusion of this first time step, solutions are analyzed against the CFL stability criteria. If any CFL criterion is violated, then: the interim solutions are discarded; the CFL coefficient and time step are re-calculated; and the time step is reset. However, provided stable solutions prevail, the second time step is executed over solution $\mathbf{U}_{i,j,k}^{n+1}$, with time step operator ordering reversed to eliminate directional bias. As in the two-dimensional case, subject to stability verification of $\mathbf{U}_{i,j,k}^{n+2}$, simulation time is advanced by $2\Delta t$ and the second-order accurate scheme is repeated until the desired solution time is achieved.

5.3.4. Special Considerations

Three-dimensional splitting facilitates solving the Euler conservation equations, in the x, y, and z directions, as

$$\begin{bmatrix} \rho \\ \rho u \\ E \\ \rho v \\ \rho w \end{bmatrix}_t + \begin{bmatrix} \rho u \\ \rho u^2 + p \\ E(u+p) \\ \rho v u \\ \rho w u \end{bmatrix}_x = \mathbf{0}, \tag{5.32}$$

$$\begin{bmatrix}\rho \\ \rho v \\ E \\ \rho u \\ \rho w\end{bmatrix}_t + \begin{bmatrix}\rho v \\ \rho v^2 + p \\ E(v+p) \\ \rho uv \\ \rho wv\end{bmatrix}_y = \mathbf{0}\,, \tag{5.33}$$

and

$$\begin{bmatrix}\rho \\ \rho w \\ E \\ \rho u \\ \rho v\end{bmatrix}_t + \begin{bmatrix}\rho w \\ \rho w^2 + p \\ E(w+p) \\ \rho uw \\ \rho vw\end{bmatrix}_z = \mathbf{0}\,. \tag{5.34}$$

As in the two-dimensional case, tangential velocities, their associated momentum fluxes, and the energy flux require special consideration. Within system (5.32), u represents the normal component of material velocity, while v and w represents the tangential, or shear, components. The normal velocity component in system (5.33) is v while u and w signify tangential components. Finally, in (5.34), w denotes the normal velocity component, while u and v correspond to tangential components.

Solutions to the aforementioned systems of equations that apply TVD flux limiter functions produce the dissipative wave structure of

Figure 5.8. As in the two-dimensional case, normal and tangential flux calculations are determined separately. Similarly, weighted average states of density, normal velocity, and

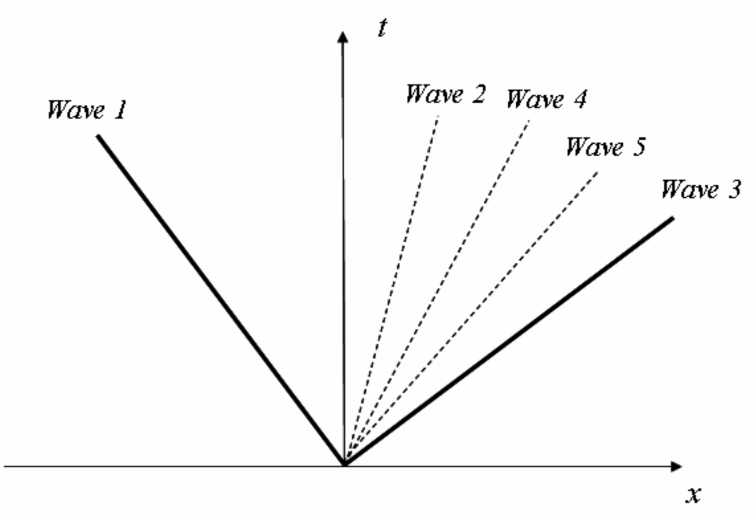

Figure 5.8. Three-Dimensional TVD Flux Limiter Wave Structure

pressure are determined using equations (4.43) and (4.44), and their corresponding fluxes are subsequently computed. Calculation of the tangential velocity weighted average states and their resultant tangential momentum fluxes is also analogous to the two-dimensional case. Specifically, if V_{T1} and V_{T2} denote the two tangential velocity components, then the weighted average states of these elements are calculated as

$$\begin{aligned} \overline{V}_{T1,i+1/2} &= \beta_{5,LWAF} V_{T1,1} + \beta_{6,LWAF} V_{T1,4} \\ \overline{V}_{T2,i+1/2} &= \beta_{7,LWAF} V_{T2,1} + \beta_{8,LWAF} V_{T2,4} \end{aligned} \tag{5.35}$$

where $\beta_{5,LWAF}$ and $\beta_{6,LWAF}$ are given by equations (5.17) and (5.18) and

$$\begin{aligned} \beta_{7,LWAF} &= (1 + \phi_5 Sign(c_5)), \\ \beta_{8,LWAF} &= (1 - \phi_5 Sign(c_5)). \end{aligned} \tag{5.36}$$

Conveniently, the eigenvalue structure of solutions to (5.32) – (5.34) dictates $c_5 = c_4 = c_2$ and, like ϕ_4 , the weight limiter function ϕ_5 is calculated from its tangential velocity gradients ΔV_{T2} as in equation (5.19). Hence, calculation of all components required to solve the three-dimensional time dependent Euler conservation equations is complete.

5.3.5. Sod Test in Three Dimensions

The benchmark shock tube test is re-visited here for the final time, to verify correct modeling of planar flows in three dimensions. The three dimensional Sod test was executed over the cubic domain [0, 1m] x [0, 1m] x [0, 1m] consisting of 100 cells in the x, y, and z directions and a diaphragm, positioned along the plane $x = 0.5$ m. Initial conditions were established as

$$\mathbf{W}(x,y,z,0) = \begin{cases} \mathbf{W}_L = (1.000\ \text{kg/m}^3, 0.0\,\text{m/sec}, 0.0\,\text{m/sec}, 0.0\,\text{m/sec}, 1.0\,\text{N/m}^2) & x < 0.5\text{m}, \\ \mathbf{W}_R = (0.125\,\text{kg/m}^3, 0.0\,\text{m/sec}, 0.0\,\text{m/sec}, 0.0\,\text{m/sec}, 0.1\,\text{N/m}^2) & x > 0.5\text{m}. \end{cases} \tag{5.37}$$

and solutions developed over the time interval t = [0, 0.25 sec]. The density profile at $t = 0.25$ sec, through the plane $z = 0.5$m is depicted in Figure 5.9 and is consistent with expected results. As in the two-dimensional case, correct modeling of planar flows was verified by comparing data extracted from the first set of cells in the y-direction against the exact solution and the second-order accurate solution obtained by the LWAF method in a single dimension. Again, the second-order accurate solutions appeared graphically identical for both the one and three-dimensional cases, and I conclude that the developed computational model accurately models planar flows.

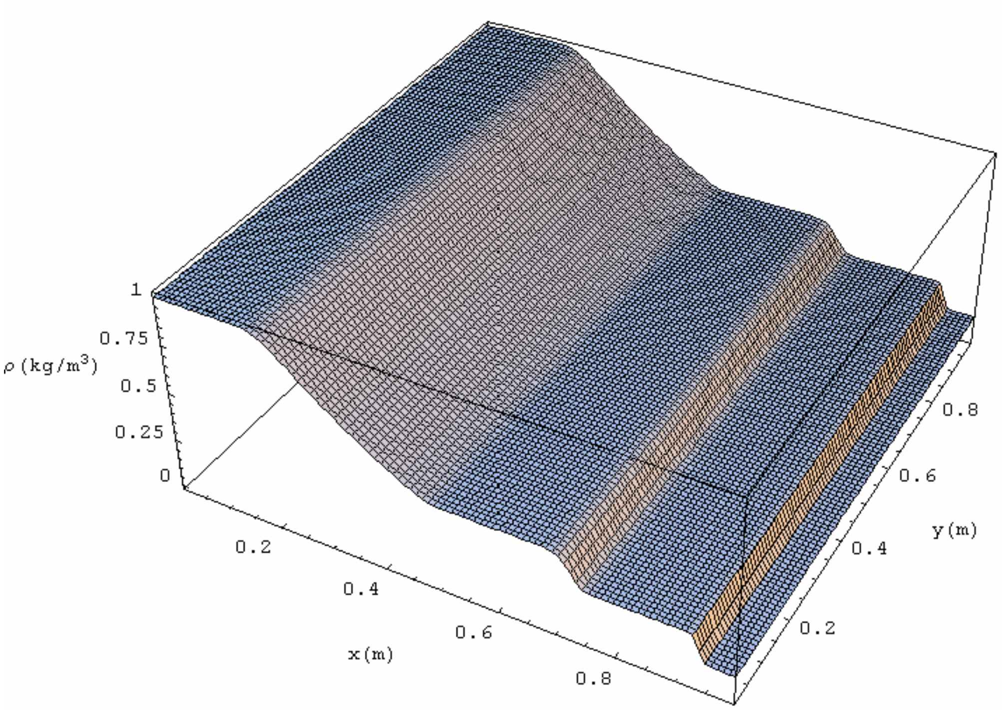

Figure 5.9. Three-Dimensional Sod Density Profile ($z = 0.5$m) at $t = 0.25$ sec

5.3.6. Mild Spherical Shock Test

To verify that the developed code correctly models flows in three dimensions, the Euler equations were solved over the cubic domain [0, 2m] x [0, 2m/ x [0, 2m] discretized as a computational mesh of 100 cells in the *x, y*, and *z* directions. Initial conditions consisted of a spherical region with radius 0.4m, centered at (1,1,1), with primitive variables of $\boldsymbol{W}_L$ and $\boldsymbol{W}_R$ from (5.37) representing states inside and outside the sphere, respectively (Toro, 1999:587). Figure 5.10 shows the density profile through the plane $z = 1$ m at $t = 0.25$ sec and indicates, as expected, a solution which exhibits a spherical shock, contact surface, and rarefaction.

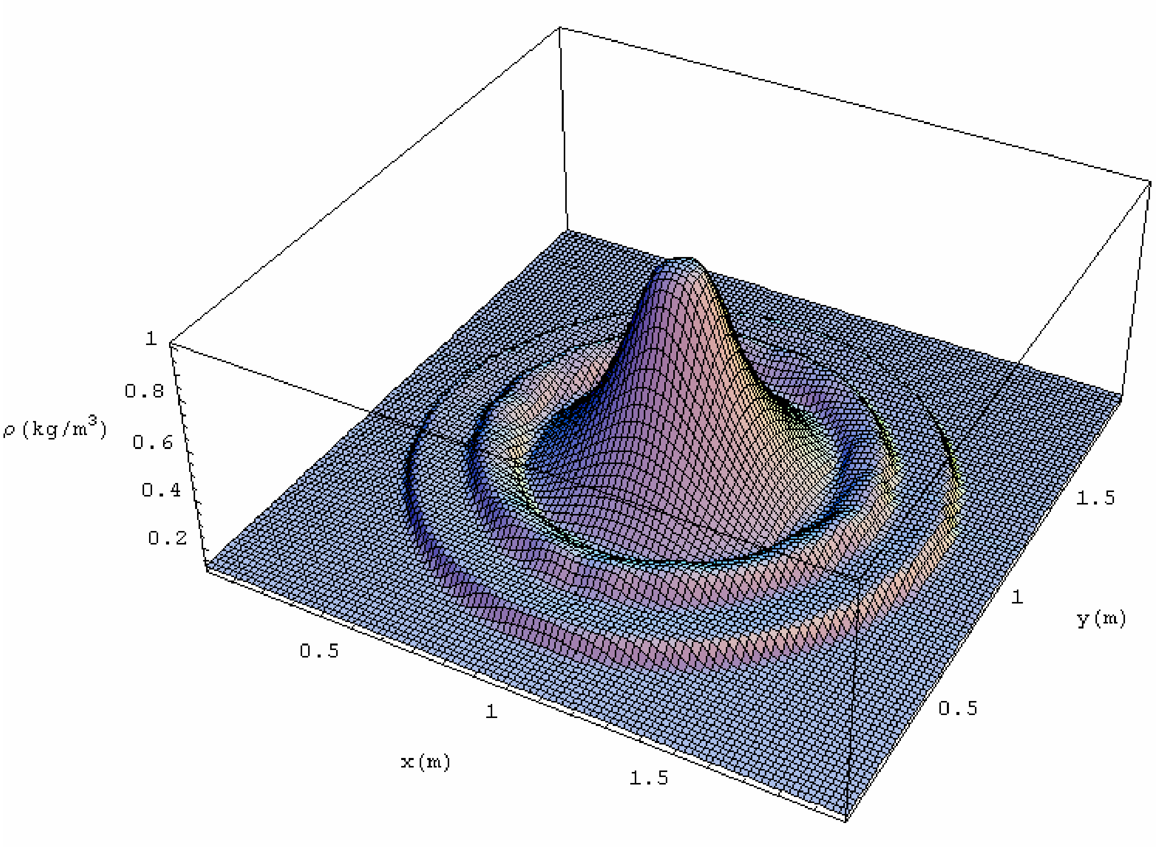

Figure 5.10. Spherical Explosion Density Profile ($z = 1$m) at $t = 0.25$ sec

As in the two-dimensional case, the density profile indicates the presence of potential numerical artifacts in the region between the rarefaction and contact discontinuity. Accordingly, a similar analysis of contour plots and mesh refinement was conducted. Increasing cells in all three directions reduced the oscillations in the region of concern and yielded improved circular symmetry.

Furthermore, densities compared along a line extending, radially, one meter outward from (1,1,1), in the plane $z = 1$ m, at angles of $\theta = 0, \pi/4, \pi/2, 3\pi/4$, and π, as measured from the x-axis. Figure 5.11 shows the density profiles along each of these lines and indicates nearly identical values for each angle.

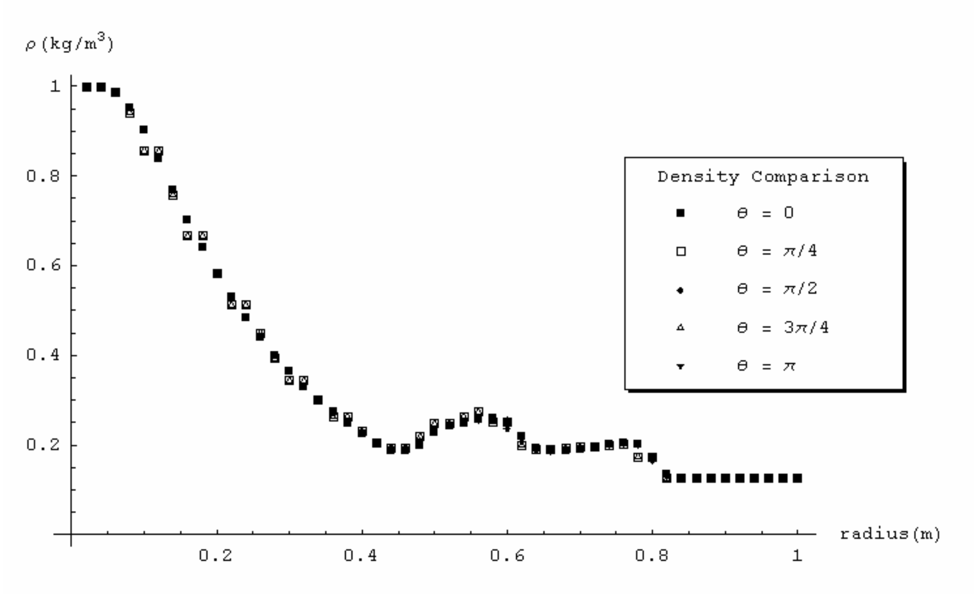

Figure 5.11. Spherical Explosion Density Comparison ($z = 1$) at $t = 0.25$ sec

To confirm spherical symmetry, similar analyses were conducted through planes $y = 1$ m and $x = 1$ m. Figure 5.12 and Figure 5.13 show the density profiles through the planes $y = 1$ m and $x = 1$ m, respectively, at $t = 0.25$ sec and are consistent with the solution presented in Figure 5.10. Densities were compared along a line extending, radially, one meter outward from (1,1,1), in the plane $y = 1$ m, at angles $\phi = 0, \pi/4, \pi/2, 3\pi/4$, and π, as measured from the x-axis. Figure 5.14 shows these density profiles along each of these lines and indicates nearly identical values for each angle. Finally, Figure 5.15 depicts identical densities plotted along a one meter radial line, extended from (1,1,1), in the plane $x = 1$ m, at angles $\Omega = 0$, $\pi/4$, $\pi/2$, $3\pi/4$, and π, measured from the y-axis. Based on these analyses, I conclude multi-dimensional flows are properly modeled using dimension splitting techniques.

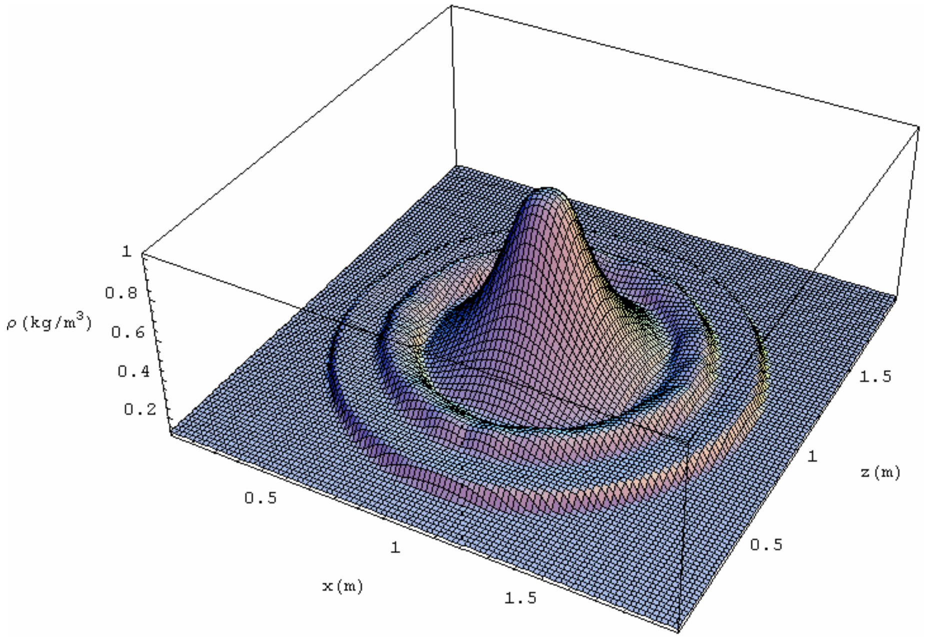

Figure 5.12. Spherical Explosion Density Profile ($y = 1$m) at $t = 0.25$ sec

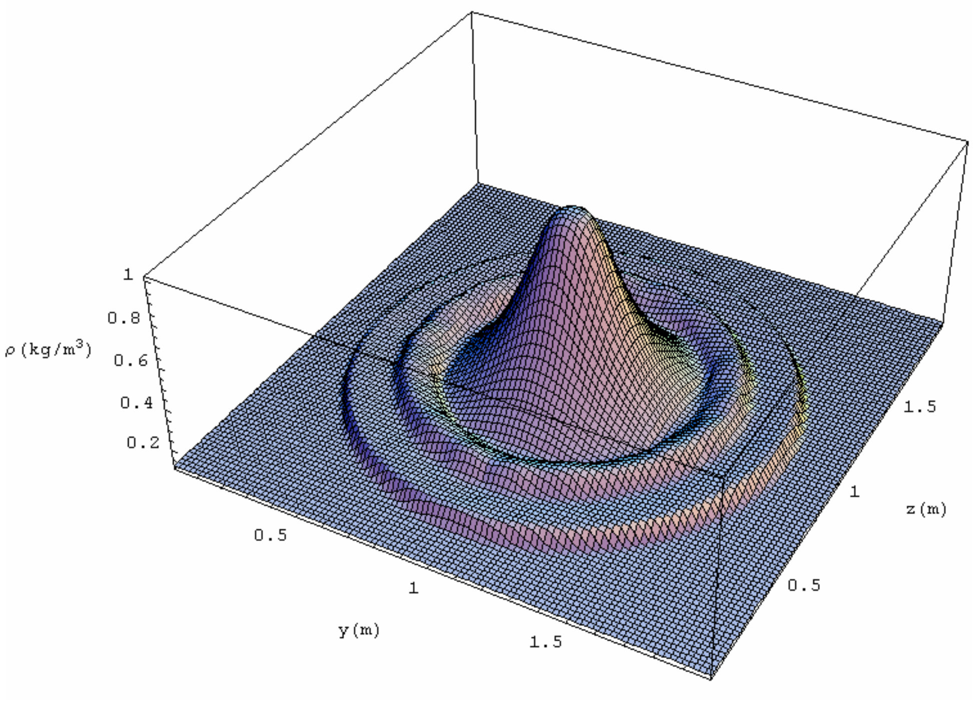

Figure 5.13. Spherical Explosion Density Profile ($x = 1$m) at $t = 0.25$ sec

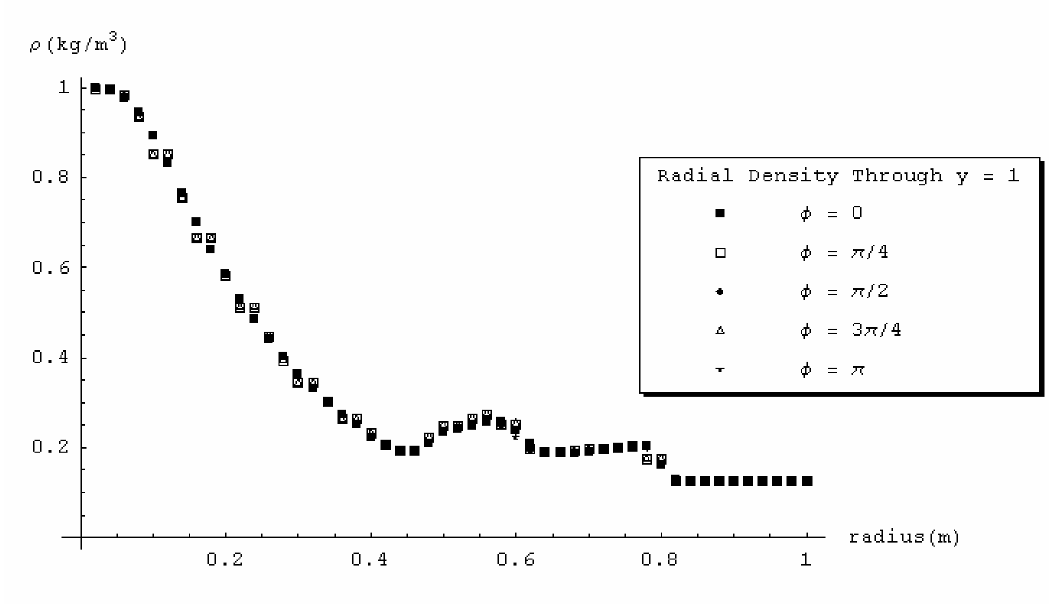

Figure 5.14. Spherical Explosion Density Comparison ($(y = 1\text{m})$) at $t = 0.25$ sec

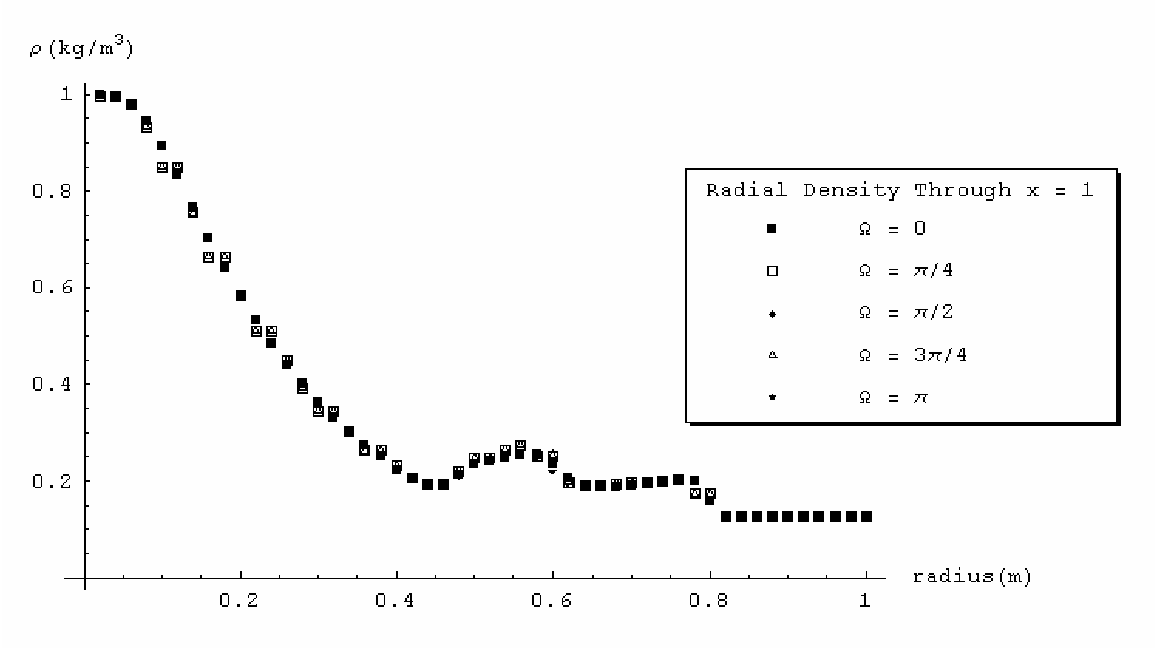

Figure 5.15. Spherical Explosion Density Comparison ($(x = 1\text{m})$) at $t = 0.25$ sec

6. Conclusion

The principal endeavor of this research was development of a three-dimensional hydrodynamic shock code to solve the Euler conservation equations, while the secondary objective included applying the developed code to model air blast propagation.

To that end, a one-dimensional, second-order accurate computational model was methodically developed, tested, and validated. Godunov's scheme executed with exact and approximate Riemann solvers, and applied to varying shock tube tests, accurately predicted wave structure and locations. Although both solvers yielded comparable accuracy, the adaptive, approximate solver improved computational efficiency by nearly 36%. Application of E.F. Toro's weighted average flux method produced second-order accuracy, but introduced false fluctuations near discontinuous regions. These oscillations were effectively reduced via TVD weight limiting techniques, where van Leer's limiter most favorably controlled behavior in the presence of shocks. The fully developed second-order accurate model was tested and verified against the ARL 57 *cm* shock tube test, and agreed with the published experimental data within 5.9%.

Following validation in a single dimension, the developed code was extended into two and three dimensions. During both implementations, output from the multi-dimensional models was compared against Sod's shock test, to verify accurate modeling of planar flows, and evaluated against mild cylindrical and spherical shock tests, presented by Toro, to confirm correct flow representation in two and three dimensions.

The end result of this research effort is a fully developed three-dimensional air blast propagation model that may be implemented, using parallel computations, to permit a more accurate and efficient exploration of air blast propagation.

Bibliography

Ben-Artzi, Matania and Falcovitz, Joseph. *Generalized Riemann Problems in Computational Fluid Dynamics.* Cambridge: The Cambridge University Press, 2003.

Bridgman, Charles J. *Introduction to the Physics of Nuclear Weapons Effects.* Virginia: Defense Threat Reduction Agency, 2001.

Burden, Richard L. and Faires, Douglas J. *Numerical Analysis, 8th Edition.* California: The Thompson Corporation, 2005.

Chang, Tung and Hsiao, Ling. *The Riemann Problem and Interaction of Waves in Gas Dynamics.* New York: Wiley, 1989.

Chorin, A.J. and Marsden, J.E. *A Mathematical Introduction to Fluid Dynamics.* New York: Springer-Verlag, 1990.

Einfeldt, B. and others. "On Godunov-Type Methods near Low Densities," *Journal of Computational Physics*: 92:273-295 (1991).

Glasstone, Samuel and Dolan, Thomas. *The Effects of Nuclear Weapons.* Washington, DC: United States Government Printing Office, 1977.

Godunov, Sergei K. "A Finite-Difference Method for the Numerical Computation of Discontinuous Solutions of the Equations of Fluid Dynamics," *Mater Sb.*: 271:1187- (1959).

LeVeque, Randall J. *Numerical Methods for Conservation Laws.* Boston: Birkhauser-Verlag, 1992.

Polyanin, Andrei D. and Zaitsef, Valentin F. *Handbook of Nonlinear Partial Differential Equations.* Florida: Chapman and Hall / CRC, 2004.

Schraml, Stephen J., *A One-Dimensional Numerical Method for Simulating Multiple Stage Shock Tube Flows.* Army Research Laboratory, Aberdeen Proving Ground, MD, November 1996 (ARL-TR-1255).

Slater, John W., "Examining Spatial Convergence – The NPARC Verification and Validation Archive," ASME Paper 2000-FED-11233, June 2000. http://www.grc.nasa.gov/WWW/wind/valid/tutorial/spatconv.html.

Toro, Eleuterio F. *Riemann Solvers and Numerical Methods for Fluid Dynamics.* New York: Springer-Verlag, 1999.

Wittig, Mark P. *Implementation of a Two-Dimensional Hydrodynamic Shock Code Based Upon the Weighted Average Flux Method.* MS Thesis, AFIT/GAP/ENP/99J-02. Air Force Institute of Technology, Wright-Patterson AFB, OH. June 1999 (ADA365941).

Woodward, P. and Colella, P. "The Numerical Simulation of Two-Dimensional Fluid Flow with Strong Shocks," *Journal of Computational Physics*: 54:115-173 (1984).

REPORT DOCUMENTATION PAGE

Form Approved
OMB No. 074-0188

1. REPORT DATE *(DD-MM-YYYY)* *15 March 2006*	**2. REPORT TYPE** Master's Thesis	**3. DATES COVERED** *(From – To)* Jun 2004-Mar 2006

4. TITLE AND SUBTITLE
Development of a Three-Dimensional Air Blast Propagation Model Based Upon the Weighted Average Flux Method

5a. CONTRACT NUMBER

5b. GRANT NUMBER

5c. PROGRAM ELEMENT NUMBER

6. AUTHOR(S)
McHale, Stephen R., MAJ, USA

5d. PROJECT NUMBER

5e. TASK NUMBER

5f. WORK UNIT NUMBER

7. PERFORMING ORGANIZATION NAMES(S) AND ADDRESS(S)
Air Force Institute of Technology
Graduate School of Engineering and Management (AFIT/EN)
2950 Hobson Way
WPAFB OH 45433-7765

8. PERFORMING ORGANIZATION REPORT NUMBER
AFIT/GNE/ENP/06-04

9. SPONSORING/MONITORING AGENCY NAME(S) AND ADDRESS(ES)
N/A

10. SPONSOR/MONITOR'S ACRONYM(S)

11. SPONSOR/MONITOR'S REPORT NUMBER(S)

12. DISTRIBUTION/AVAILABILITY STATEMENT
APPROVED FOR PUBLIC RELEASE; DISTRIBUTION UNLIMITED

13. SUPPLEMENTARY NOTES

14. ABSTRACT

Accurate numerical modeling of complex, multi-dimensional shock propagation is needed for many Department of Defense applications. A three-dimensional code, based upon E.F. Toro's weighted average flux (WAF) method has been developed, tested, and validated. Code development begins with the introduction and application of all techniques in a single dimension. First-order accuracy is achieved via Godunov's scheme using an exact Riemann solver. Adaptive techniques, which employ approximate solutions, are implemented to improve computational efficiency. The WAF method produces second-order accurate solutions, but introduces spurious oscillations near shocks and contact discontinuities. Total variation diminishing (TVD) flux and weight limiting schemes are added to reduce fluctuation severity. Finally, the fully developed one-dimensional code is validated against experimental data, and extended into two and three dimensions via dimension-splitting techniques.

15. SUBJECT TERMS
Three-Dimensional Flow, Numerical Methods and Procedures, Weighting Functions, Shock Tests

16. SECURITY CLASSIFICATION OF:			**17. LIMITATION OF ABSTRACT**	**18. NUMBER OF PAGES**	**19a. NAME OF RESPONSIBLE PERSON** **Dr. Kirk A. Mathews GNE/ENP**
REPORT U	**ABSTRACT** U	**c. THIS PAGE** U	UU	112	**19b. TELEPHONE NUMBER** *(Include area code)* (937) 785-3636 x 4508

Standard Form 298 (Rev: 8-98)
Prescribed by ANSI Std. Z39-18